Electronic Supplementary Information (ESI)

Thermodynamically controlled chemical regeneration of spent battery cathodes using recyclable electron donors under ambient conditions

Sunghyun Ko,†[ab] Jinkwan Choi,†[ac] Jihyun Hong,*[d] Changsoo Kim,[e] Uichan Hwang,[af] Minhyung Kwon,[af] Gukhyun Lim,[cd] Seok Su Sohn,[c] Jinha Jang,[b] Ung Lee,[egh] Chan Beum Park,[b] Minah Lee*[a]

[a] Energy Storage Research Center, Korea Institute of Science and Technology (KIST), 14 Gil 5 Hwarang-ro, Seongbuk-gu, Seoul 02792, Republic of Korea.

[b] Department of Materials Science and Engineering, Korea Advanced Institute of Science and Technology, 335 Science Road, Daejeon 305-701, Republic of Korea.

[c] Department of Materials Science & Engineering, Korea University, 145 Anam-ro, Seongbuk-gu, Seoul 02841, Republic of Korea

[d] Energy Materials Research Center, Korea Institute of Science and Technology (KIST), 14 Gil 5 Hwarang-ro, Seongbuk-gu, Seoul 02792, Republic of Korea.

[e] Clean Energy Research Center, Korea Institute of Science and Technology (KIST), 14 Gil 5 Hwarang-ro, Seongbuk-gu, Seoul 02792, Republic of Korea.

[f] Department of Chemical & Biological Engineering, Korea University, 145 Anam-ro, Seongbuk-gu, Seoul 02841, Republic of Korea

[g] Division of Energy and Environmental Technology, KIST School, Korea University of Science and Technology (UST), Seoul, 02792, Republic of Korea

[h] Green School, Korea University, 145 Anam-ro, Seongbuk-gu, Seoul, 02841, Republic of Korea.

† These authors contributed equally to this work.

* E-mail: minahlee@kist.re.kr (M. L.), jihyunh@kist.re.kr (J. Hong.)

Experimental details

Materials

5,10-Dihydro-5,10-dimethylphenazine (TCI, 99%), ferrocene (Aldrich, 98%), N,N-diphenyl-p-phenylenediamine (Aldrich, 98%), 1,4-di-tert-butyl-2,5-dimethoxybenzene (AA Blocks, 95%), lithium peroxide (Aldrich, 90%), and lithium sulfide (Aldrich, 99.98%) were used as received and stored in an Ar-filled glove box (Korea Kiyon, MOTek, H_2O<0.1 ppm, O_2<5 ppm). 1,2-dimethoxyethane (DME, Aldrich, 99.5%) and 2-methyl-tetrahydrofuran (2-meTHF, Aldrich, 99%) were dried overnight using a molecular sieve (Alfa, pore size: 3 Å) before use. Lithium bis(tri-fluoromethanesulfonyl)imide (LiTFSI, Aldrich, 99.95%) was kept at 110 °C using a hot plate overnight under vacuum. 1 M $LiPF_6$ in ethylene carbonate (EC)/diethyl carbonate (DEC) (1:1 vol%) (Panax Etec Co., Ltd., Korea) was used as received without any further treatment.

Preparation of Li-deficient cathodes

For the fabrication of the NMC622 electrodes, $LiNi_{0.6}Mn_{0.2}Co_{0.2}O_2$ (NMC622, Wellcos Corporation, Korea), Super P carbon black (MTI, Korea), and polyvinylidene fluoride (PVDF) binder in a weight ratio of 85:5:10 were dissolved in N-methyl-2-pyrrolidone (NMP) and mixed using a planetary centrifugal mixer (THINKY Corporation, Japan). The resulting slurry was cast on carbon-coated aluminum foil with an areal loading of 5 mg cm^{-2} and dried in a vacuum oven at 80 °C. The high-loading NMC622 electrode was prepared by mixing NMC622, MWCNT, PVDF, and dispersant in a weight ratio of 96.5:1:2.3:0.2, and cast on the Al foil with an areal capacity of 3 mAh cm^{-2} (17 mg cm^{-2}). For double-coated NMC622 electrodes, the slurry was coated on both sides of carbon-coated aluminum foil with an areal active loading of 10 mg cm^{-2}. The dried NMC622 electrodes were roll-pressed and punched into a diameter of 11.3 mm (1.003 cm^2). The $LiFePO_4$, $LiNi_{0.5}Mn_{1.5}O_4$, and $LiCoO_2$ active materials were mixed with Super P carbon black and PVDF binder in weight ratio of 70:20:10, 80:10:10, and 80:10:10, respectively. After that, electrodes were prepared in the same way as NMC622 electrodes.

The Li-deficient cathodes were prepared by galvanostatically charging (without a constant voltage hold) the fresh electrodes to the targeted SOC. The electrodes were assembled into 2032-type coin cells with a polymer separator (Celgard 2320) and Li metal. 1 M $LiPF_6$ in EC/DEC (1:1 vol%, 30 µl) was used as the electrolyte. After cycling at 0.1C (18 mA g^{-1}) for two cycles, the cell was charged to 15%, 30%, 45%, or 90% SOC to form a targeted amount of V_{Li} in the electrode. For the double-coated NMC622, the electrode (2×2 cm^2) was assembled into a pouch cell using Li deposited Cu foils as the anode for both sides and charged to 30% SOC at 0.1C after two formation cycles.

Thermodynamically controlled chemical regeneration of Li-deficient cathode

The regeneration solutions were prepared by simply mixing the RED and Li salt (LiTFSI or $LiPF_6$) in the solvent (DME or 2-meTHF). The solution contained 1.5–10 times more RED and Li salt than the V_{Li} in NMC. The concentration of RED and Li salt in the regeneration solution ranged from 21 to 150 mmol L^{-1}. To demonstrate the RED-based chemical regeneration, the Li-deficient cathode was immersed in the regeneration solution for a controlled duration and temperature. The cathode was then rinsed with 1 ml of the pure solvent (DME or 2-meTHF) to remove the residual REDs and Li salts from the regeneration solution.

Recycling of used regeneration solution

To demonstrate recyclability of the regeneration solution, the DME solution containing 50% excess DMPZ and LiTFSI compared with the V_{Li} in NMC622 was prepared as an example. The used regeneration solution was collected after the lithiation of Li-deficient NMC622 for 2 hours in an Ar-

filled glove box. Then, Li_2O_2 were added to the used regeneration solution. The molar ratio of Li_2O_2/DMPZ was 120 in this demonstration. After stirring overnight, the supernatant was selectively collected using a PTFE syringe filter with a pore size of 0.1 μm. Another Li-deficient NMC622 cathode was immersed in the recycled DMPZ solution for 2 hours to demonstrate the reusability of the solution. We also used Li_2S as the reducing agent and Li source for solution recycling. For reducing chemical waste, 0.6 molar equivalent of Li_2S (Li/RED = 1.2) was used to reduce oxidized RED in this case.

Electrochemical measurements

OCV monitoring in a three-electrode system was conducted using a compact potentio-galvanostat (PalmSens4, Netherlands) in an Ar-filled glovebox at room temperature. Li-deficient NMC622 was prepared (30% SOC, as described above) and used as a working electrode. A Pt coil was used as a counter electrode while avoiding physical contact with the NMC622 electrode to prevent short-circuit. A piece of Li metal (0.3×0.3 cm^2) separated by a glass frit was used as a reference electrode. All the electrodes were immersed in a DME solution containing only LiTFSI and allowed to rest for 4 min while stirring. An equimolar amount of DMPZ in DME was injected into the LiTFSI solution.

The regenerated NMC622 electrode was assembled into a 2032 type Li half-cell configuration with a polymer separator (Celgard 2320) and Li-metal anode. A total volume of 30 μl of 1 M $LiPF_6$ in EC/DEC (1:1 vol%) was used as the electrolyte. The assembled coin cells were loaded into a battery cycler (WBCS-3000, Wonatech Co. Ltd., Korea). Long-term cyclability was tested by galvanostatic cycling without a constant voltage holds, where the charging and discharging C-rates were identical after three formation cycles at 0.1C (1C=180 mA g^{-1}). The rate capability tests were carried out at different rates (0.5C, 1C, 2C, and 3C) after the activation cycles at 0.1C, without applying a constant voltage holds. Potential-controlled electrochemical impedance spectroscopy (EIS) was conducted on half cells in a frequency range of 1 MHz to 100 mHz with an AC voltage perturbation of 10 mV (BioLogic, France). To measure resistance in the equilibrium state, EIS were conducted 1 hour after reaching the target voltage of 4.3 V (vs. Li/Li^+). To minimize sample-to-sample variations, the EIS spectrum was obtained for the same cathode before and after regeneration.

Cyclic voltammograms of each RED was collected with the coin cells using stainless-steel plate (thickness of 0.5 mm and diameter of 16mm) as a cathode instead of an NMC622 electrode. In addition, 30 μl of DME solution containing RED (21 mmol L^{-1}) and LiTFSI (22.5 mmol L^{-1}) was used as the electrolyte.

To harvest the cycled NMC811 materials from the pouch cells, the commercial 1-Ah-capacity pouch cells (Remplir, Korea) were cycled within the voltage range of 4.2–2.75 V (vs. Li/Li^+). 1 M $LiPF_6$ in EC/DEC (1:1 vol) with 3 vol% VC (and 3 vol% FEC) was used as an electrolyte. To prepare the degraded NMC811 cathode with a 20% capacity loss, the pouch cell was initially cycled for three cycles at 0.1C (90 mA), followed by extended cycling at 0.5C for 820 cycles at 30 °C. To obtain even more degraded samples (60% capacity loss), another pouch cell was cycled at 2C for 400 cycles after three formation cycles at 50 °C. After galvanostatic cycling, the pouch cell was discharged to 2 V for safety concerns and then disassembled in an Ar-filled glove box. The NMC811 cathodes were washed with dimethyl carbonate (DMC) and scraped with a stainless-steel spatula to collect cycled NMC811 materials. The fresh powder sample was obtained from a fresh pouch cell after formation cycles. The lithiation of the cycled NMC811 powder (500 mg) was performed in a dry room (dewpoint under −50 °C) environment using the regeneration solution (15 ml) containing three times more DMPZ and LiTFSI than V_{Li} in the cycled NMC811. After stirring for 2 hours at room temperature, the regenerated NMC811 powder was thoroughly washed with DME using the same volume of the regeneration solution and subsequently dried under vacuum. For the electrochemical tests of the harvested powders (fresh, cycled, and

regenerated NMC811) the sample was mixed with extra Super P carbon black and PVDF in NMP at a final ratio of 90:5:5. After that, electrodes were prepared in the same way as NMC622 electrodes.
For the full-cell demonstration, an aqueous slurry composed of graphite (SMG A-5, Hitachi, Japan), Super P carbon black (MTI, Korea), and binder (LPIMAM37B, Aekyung Chemical Co., Ltd. Korea) with a mass ratio of 85:5:10 was mixed using a planetary centrifugal mixer. The resulting slurry was cast on surface-etched copper foil and dried in a vacuum oven at 120 °C. The dried graphite electrodes were roll-pressed and punched into a diameter of 12 mm (1.131 cm^2). The full cells were designed to have an N/P ratio (the practical capacity ratio of the negative electrode to the positive electrode) of 1.05. The full cells were charged and discharged at 0.1C for initial 3 cycles, followed by 1C.

Characterization of regenerated NMC

UV–Vis absorption spectra were recorded using a spectrophotometer (JASCO FP6500). Fourier-transform infrared spectroscopy (FT-IR) was performed on each electrode using ATR mode (Thermofisher Scientific Nicolet iN10MX) at a resolution of 4 cm^{-1}. 1H-NMR spectroscopy was performed on a Avance Neo (600 MHz spectrometer) using DMSO-d_6. X-ray diffraction (XRD, Rigaku SmartLab, Japan) analysis was conducted at a scan rate of 1° min^{-1} with Cu Kα radiation. For the characterization of double-side coated NMC622 electrode, XRD (Rigaku Miniflex II, Japan) analysis was conducted at a scan rate of 2° min^{-1} with Cu Kα radiation. Rietveld refinement was performed on all XRD patterns by FullProf Suite software to determine the crystal lattice parameters. The composition of the NMC622 electrodes was measured using inductively coupled plasma mass spectrometry (ICP-MS, Thermofisher Scientific ICAP RQ). Transmission electron microscopy (TEM) analysis was performed with the TEM with the probe aberration corrector, Titan 80-300TM (Thermofisher, Netherlands), and the sample particles were dropped on the Cu grids after dispersing in dimethyl carbonate (DMC). The morphology of the electrodes was observed in field-emission scanning electron microscopy (FE-SEM, Regulus 8230, Hitachi, Japan).
Synchrotron-radiation-based experiments were performed at the Pohang Accelerator Laboratory (PAL), Pohang, South Korea. Near-edge X-ray absorption fine structure spectroscopy (NEXAFS) analysis was performed at the 10D-XAS-KIST and 8A1-SPEM beamlines, operating at 3.0-GeV energy with a maximum storage current of 360 mA. All the samples were sealed with an aluminum pouch in an Ar-filled glove box and moved to the beamline to avoid air exposure. All the NEXAFS spectra were collected by subtracting the background, followed by normalization using the incident photon flux measured from gold mesh in the path of the X-ray beam.

Economic and environmental analysis of different battery recycling technologies

The EverBatt 2020 model, an Excel-based battery recycling process and supply chain model developed by Argonne National Laboratory, was used to evaluate the cost-effectiveness and environmental impact of our approach for a throughput of 10,000 tons of spent battery cells per year. For the calculation, we used Fc, DME, and LiTFSI as a RED, solvent, and Li salt, respectively, comprising our cathode regeneration solution, a combination that yields the highest cost-effectiveness and least environmental impact among our RED-based recycling conditions. To recycle 1 kg of spent NMC622 battery cell, 18.74×10^{-3}, 0.46×10^{-3}, 0.28×10^{-3}, and 14.7×10^{-3} kg of DME, LiTFSI, Fc, and Li_2S are consumed during the RED-based process, respectively. The material requirements are calculated based on our experimental demonstrations (Table S9). We compared the value with those of pyrometallurgical, hydrometallurgical methods, which we obtained from default values established in the EverBatt 2020 to recycle NMC622 from spent LIBs. As shown in Table S10, energy requirements for the RED-based process are obtained from the previous paper, which demonstrated the direct

regeneration under the comparable condition (30 °C, 0.5 hour, and ambient pressure)[1], which are also compared with those of pyrometallurgical, hydrometallurgical methods.

The process consists of cathode separation, cathode regeneration, washing, and drying steps as illustrated in Supplementary Figure S44. Based on our experiment, we also included a recycling step for the used solution which can be reused in the subsequent cathode regeneration. The immersion tank for the cathode lithiation step was assumed to comprise an industrial-scale continuously stirred tank reactor.[2] We assumed that all used reagents were retrieved with a recovery rate of 90% through the solution recycling step.

The prices of Fc, DME, LiTFSI, and Li_2S were determined based on the bulk price currently available in the market for each chemical with a purity of 99% or higher. As for the life cycle inventory (LCI) of the materials required for our RED-based process, materials that could be found in conventional databases were directly utilized, while others were approximated from previous literature or calculated from process models. The LCI for $LiPF_6$ from GREET® was used as a substitution of the LCI for LiTFSI. The LCI for 1,2-dimethoxyethane was obtained from the Ecoinvent V3 database.[3] The LCI for Fc and Li_2S were acquired by incorporating the process information provided in Griffiths et al.[4] and Keshavarzmohammadian et al.[5], respectively. Considering the uncertainty of LCI obtained by process approximation, uncertainty analysis was conducted to account for the possible variations of the mass and energy balances (Supplementary Table S12-S13). To analyze the environmental impact of these materials, the ReCiPe 2016 Midpoint (H) method was used to obtain indices such as global warming impact (GWI) and fossil resource scarcity (FRS), and the cumulative energy demand (CED) was incorporated to analyze the total amount of energy usage for producing the materials.[6]

The cost and LCA results for the pyrometallurgical and hydrometallurgical methods were obtained from the EverBatt 2020 model, where we selected NMC622 as a cathode material for the spent battery cell. The cost and LCA results for other direct regeneration methods were directly adopted from the previous papers.

In assumption of a typical annealing procedure (700°C for 2 hours, 5°C min^{-1}) following the RED-based chemical regeneration, the required heat was calculated using the following equation:[7]

$$Q = \int_0^t \left[mC_p \frac{dT}{dt} + Ah(T - T_{amb}) \right] dt$$

The first term represents the heat energy required for changing temperature of the cathode material, which is a function of the mass (m), specific heat capacity (C_p) of the cathode material, and the temperature ramping rate (dT/dt). The second term accounts for the heat energy required to maintain the temperature at the target temperature, compensating for heat loss to the surroundings (at T_{amb}) with a heat transfer coefficient (h) and the temperature difference ($T-T_{amb}$) through the surface (A) of the cathode material. The C_p (71.62 J mol^{-1} K^{-1}) and A (0.021 m^2) of $LiCoO_2$ (LCO) were used as representative values for layered oxide cathode materials.[7] We scaled the Q value of each term to correspond to the amount of heat energy needed to anneal 1 kg of spent battery cells, based on the cathode material content (35.3 wt%) as specified in the EverBatt model.

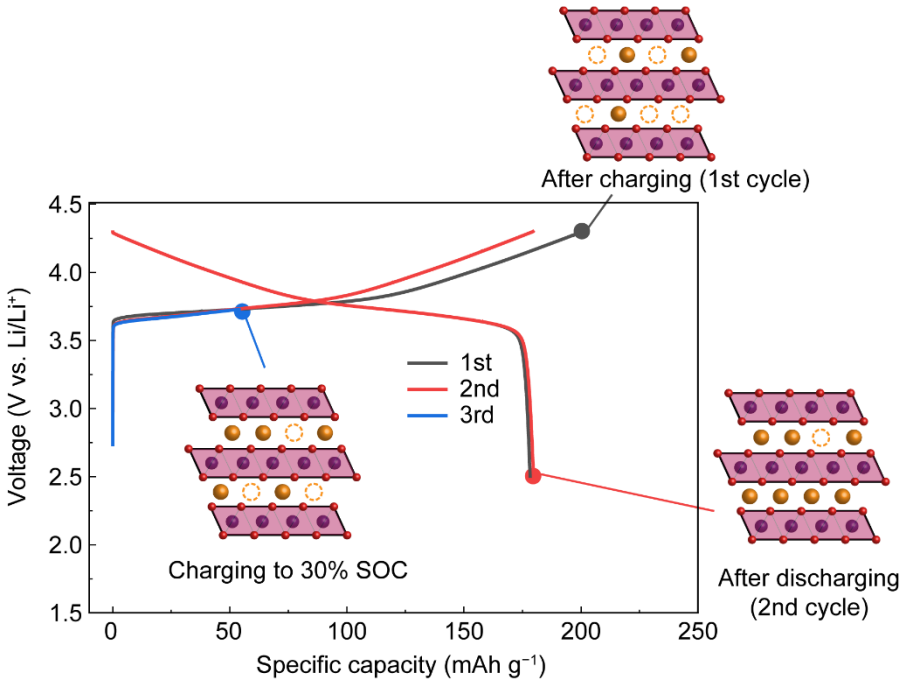

Fig. S1 Schematic illustration of V_{Li} formation process for the NMC622 cathode during formation cycles at 0.1C. The NMC622 cathode lost 7.7% Li content during the first charge/discharge cycle. The delithiation/lithiation processes are completely reversible in the second cycle, showing a CE of 100.1%. After charging to 30% SOC (54 mAh g^{-1}) in the third charge process, nearly 24.1% V_{Li} was formed in NMC622 cathode, resulting in $Li_{0.76}Ni_{0.6}Mn_{0.2}Co_{0.2}O_2$ composition.

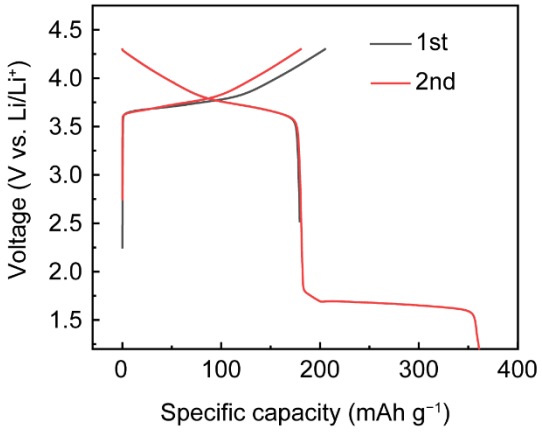

Fig. S2 Charge/discharge profiles of NMC622 in a half cell at 0.1C. At the end of the second discharge process, the cell was further discharged below 2 V (vs. Li/Li^+) and exhibited a long plateau at 1.6 V, attributable to the reduction of Mn^{4+} into Mn^{3+}.[8]

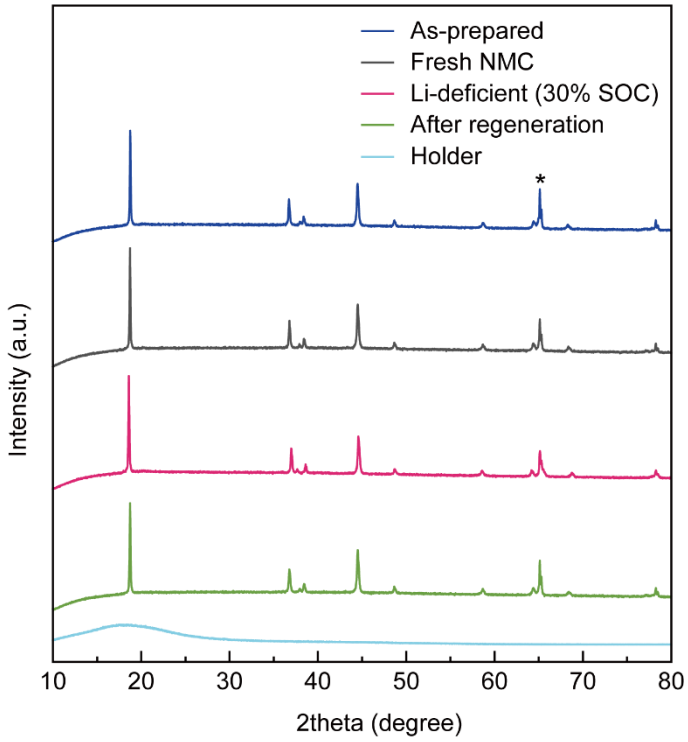

Fig. S3 Full-range XRD patterns of NMC622 cathodes at different electrochemical states. The asterisk (*) denotes a characteristic peak of Al foil (2θ = 64.86°).

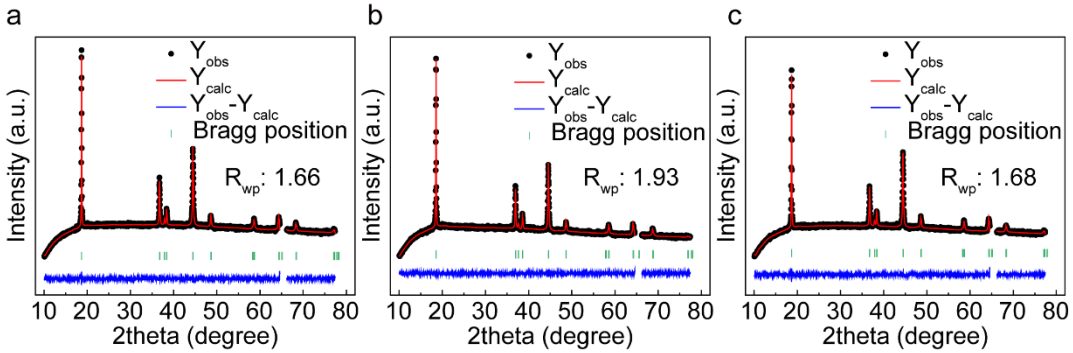

d

Sample name	Lattice parameter		
	a	b	c
Fresh	2.867 (0)	2.867 (0)	14.247 (1)
Li-deficient	2.849 (0)	2.849 (0)	14.343 (1)
Regenerated	2.867 (0)	2.867 (0)	14.248 (1)

Fig. S4 The Rietveld refinement for full-range XRD patterns of (**a**) fresh, (**b**) Li-deficient, and (**c**) regenerated NMC622 cathodes. The characteristic peaks of Al foil (2θ = 64.6 – 66.2° and 77.4 – 80.0°) were excluded for the analysis. (**d**) The lattice parameters of NMC622 cathodes obtained from the Rietveld refinements.

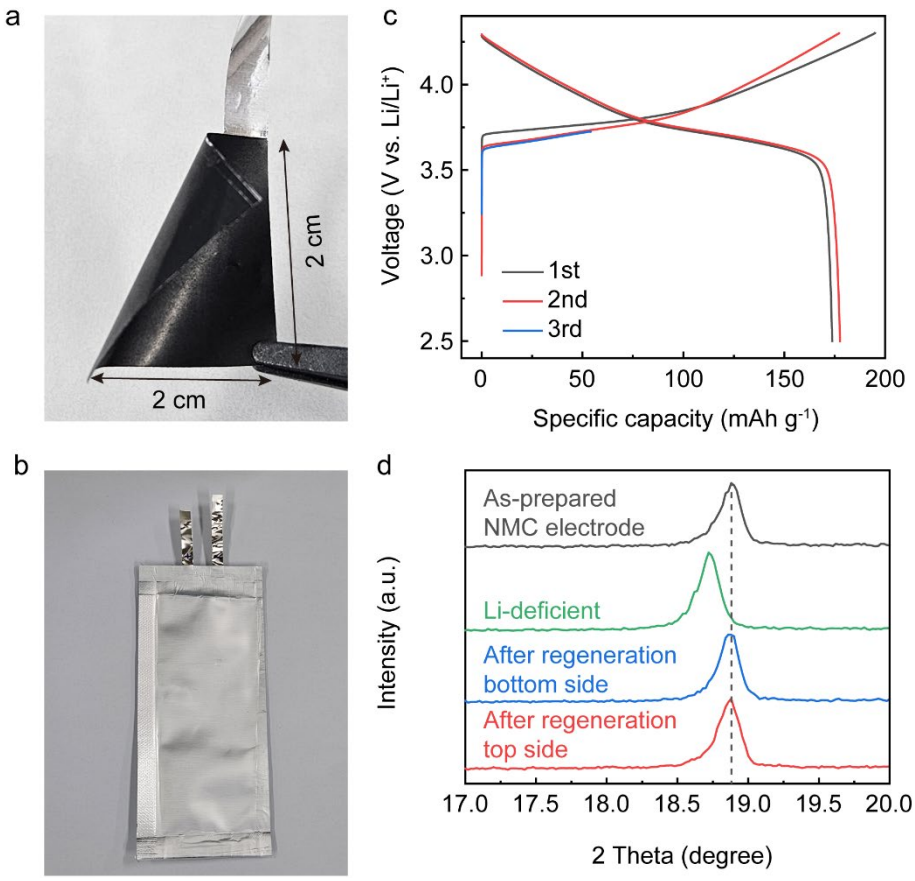

Fig. S5 Photographs of (**a**) a double-coated NMC622 cathode (2×2 cm^2) and (**b**) the pouch cell assembled with the double-coated electrode sandwiched by two pieces of the electrodeposited Li metal on Cu foil. (**c**) Charge/discharge profiles of the double-coated NMC in the pouch cell. To prepare the Li-deficient double-coated electrode, the cell was charged to 30% SOC at 0.1C after two formation cycles. (**d**) XRD patterns of the as-prepared NMC, Li-deficient NMC, and each side of regenerated NMC. The regeneration solution contains ten times more DMPZ and LiTFSI than V_{Li} in Li-deficient NMC. The reversible shift of the (003) peak after regeneration confirms the complete recovery of the Li content in the double-coated cathode.

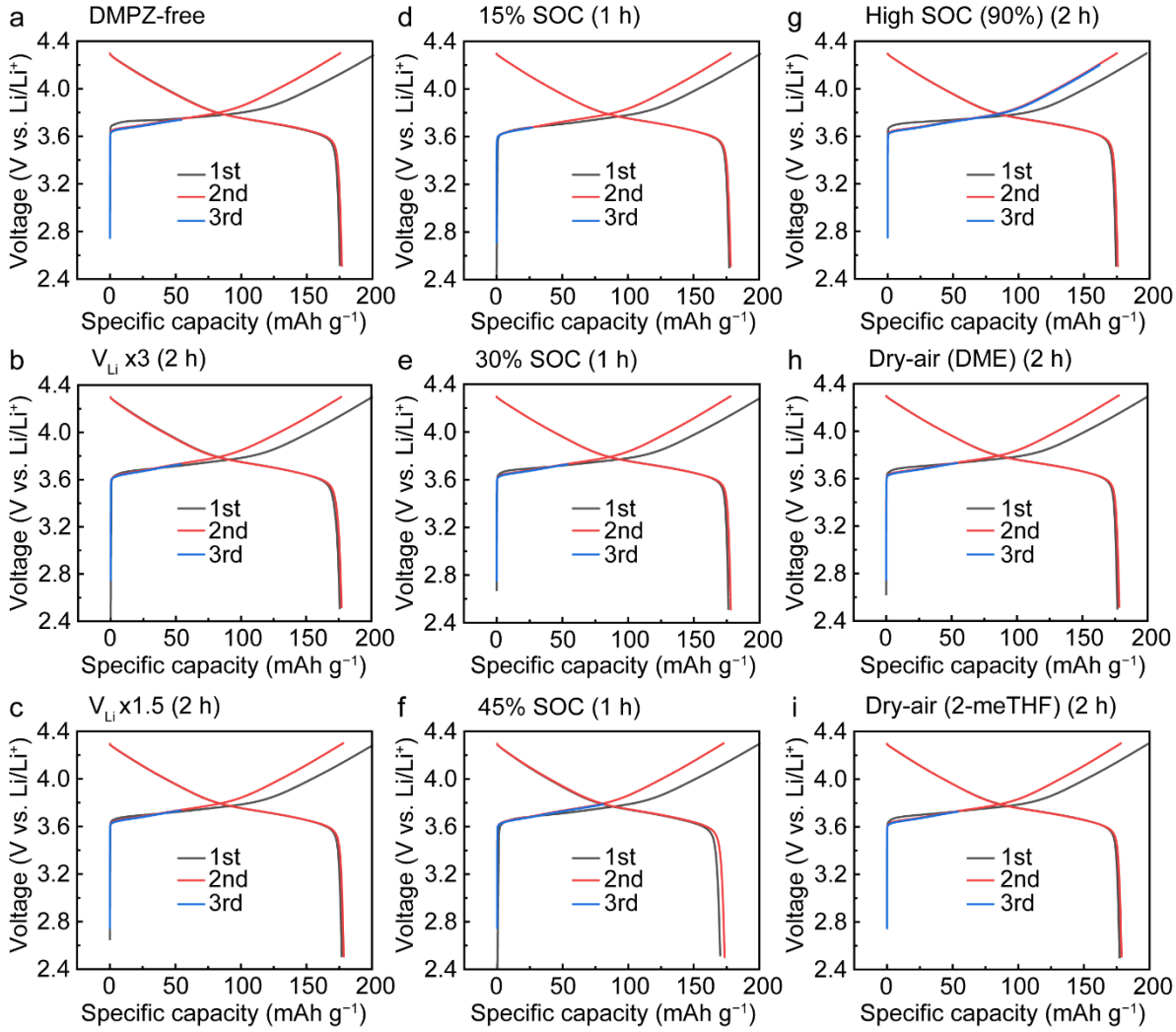

Fig. S6 Charge/discharge profiles of NMC622 cathodes for V_{Li} formation processes obtained for preparing electrodes tested in Figures 2a-2c in the main text. The Li-deficient cathodes were retrieved and regenerated under various conditions denoted as (**a**) DMPZ-free, (**b**) V_{Li} ×3, (**c**) V_{Li} ×1.5, (**d**) 15% SOC, (**e**) 30% SOC, (**f**) 45% SOC, (**g**) High SOC (90%), (**h**) Dry-air (DME), and (**i**) Dry-air (2-meTHF).

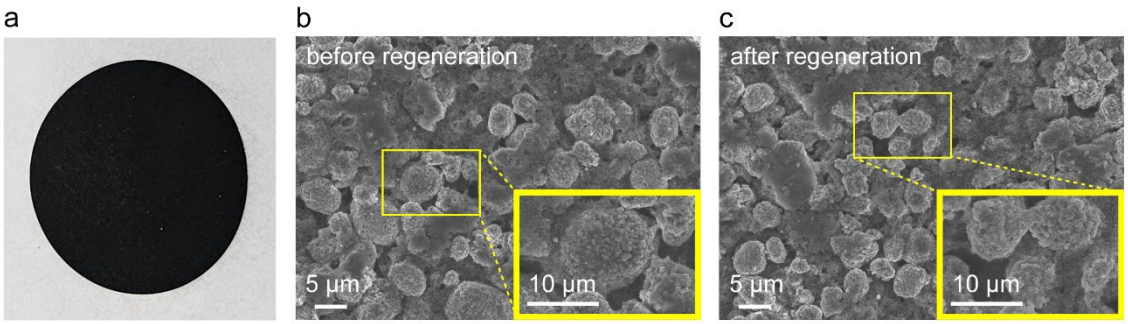

Fig. S7 (**a**) A digital photograph of the regenerated NMC622 cathode after rinsing. SEM images of (**b**) the fresh NMC622 and (**c**) the regenerated NMC622. Compared to the fresh NMC622, the regenerated cathode remained nearly intact without significant pulverization or intergranular cracking of the active particles.

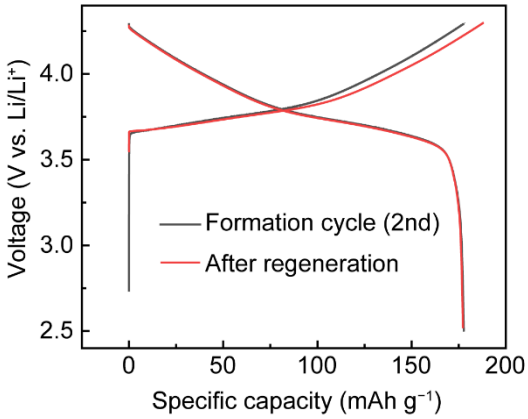

Fig. S8 Charge/discharge profiles of fresh and regenerated NMC622 cathodes with a high active material loading of 17 mg cm^{-2}. The thick electrode was immersed in a regeneration solution containing ten times more DMPZ and LiTFSI than V_{Li} in NMC622 for two hours. After regeneration, the NMC622 exhibited an initial charge capacity corresponding to 105.6% of the reversible capacity of the fresh NMC622 while showing a CE of 94.1%. This indicates that the chemical regeneration induces deep lithiation, recovering the lithium content close to 1 in $Li_xNi_{0.6}Mn_{0.2}Co_{0.2}O_2$, which can barely be achieved by electrochemical lithiation.

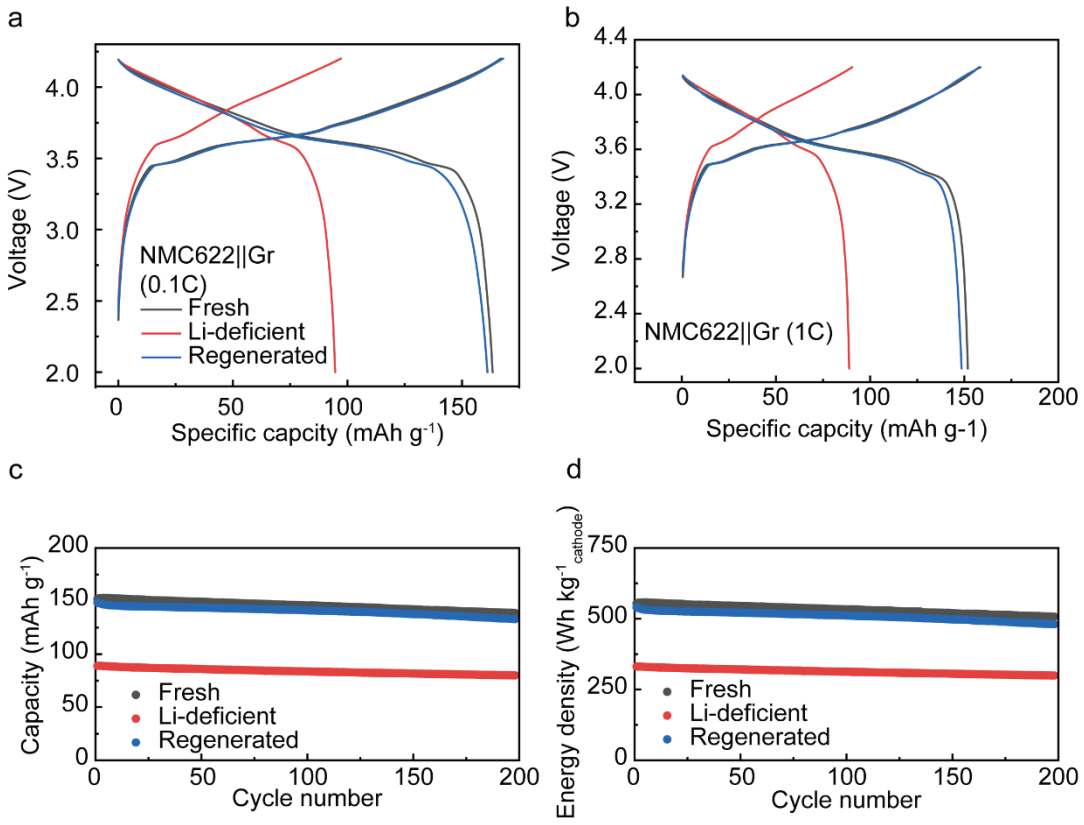

Fig. S9 Electrochemical performances of NMC622||graphite full cells assembled with NMC622 cathodes in different states (fresh, Li-deficient, and regenerated) and fresh graphite (Gr) anodes. Voltage profiles of the full cells at (**a**) 0.1C and (**b**) 1C. The long-term cycling test was conducted at 1C after three formation cycles at 0.1C within the voltage range of 4.2–2.0 V. The retentions of (**c**) the discharge capacity and (**d**) energy density after the formation cycle. In the full cells, the Li-deficient and regenerated NMC622 cathodes exhibited 58% and 99% of the original capacity from the fresh NMC622 cathode at 0.1C. After 200 cycles, the full cells exhibited similar capacity retention of 91%, 90%, and 89% for fresh, Li-deficient, and regenerated NMC622, respectively. The full cell of the regenerated NMC622 cathode exhibited 98% energy density of the fresh NMC622 cathode, proving the effectiveness of our RED-based regeneration.

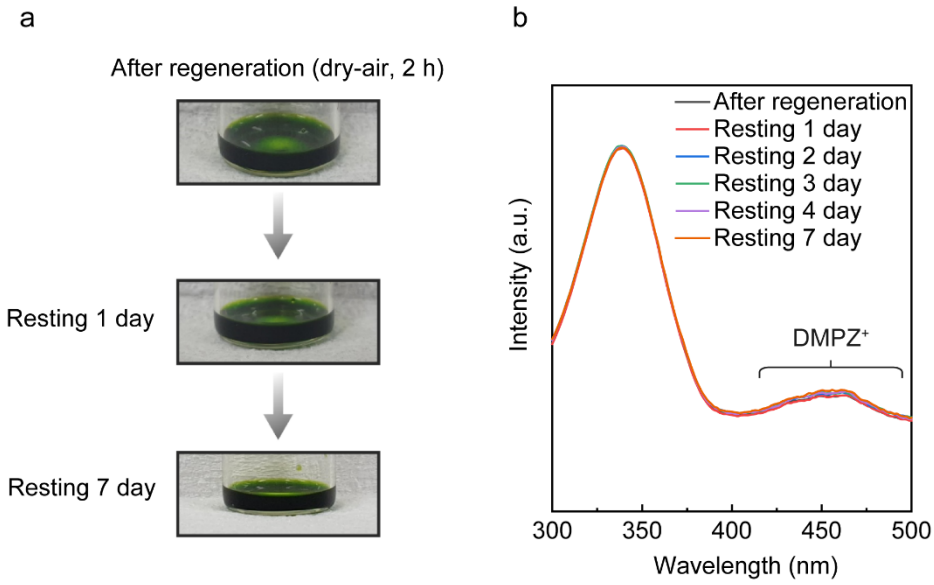

Fig. S10 (**a**) Photographs of the DMPZ solution after treating the Li-deficient NMC622 in dry air. The DMPZ solution contained ten times more DMPZ and LiTFSI than V_{Li} in NMC622. No color change was observed in the regeneration solution during resting in a dry room for one week. (**b**) UV–vis absorption spectra of the regeneration solution during exposure to dry air. The characteristic peaks of $DMPZ^+$ (420–480 nm) were well maintained without any sign of a side reaction peak.

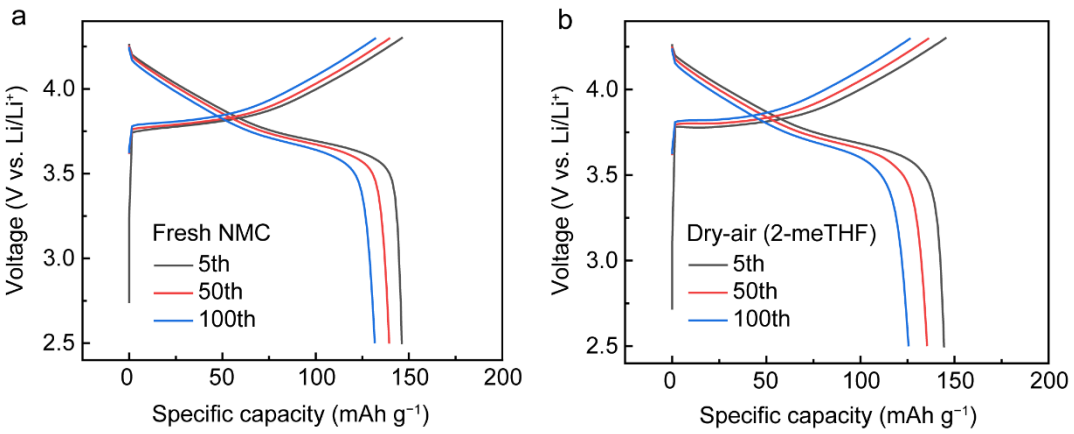

Fig. S11 Charge/discharge profiles for the 5th, 50th, and 100th cycles during long-term cycling (3C) of (**a**) fresh NMC and (**b**) NMC regenerated under "Dry-air (2-meTHF)" condition. The regenerated cathode exhibited a capacity retention higher than 85% after 100 cycles, comparable to the fresh cathode.

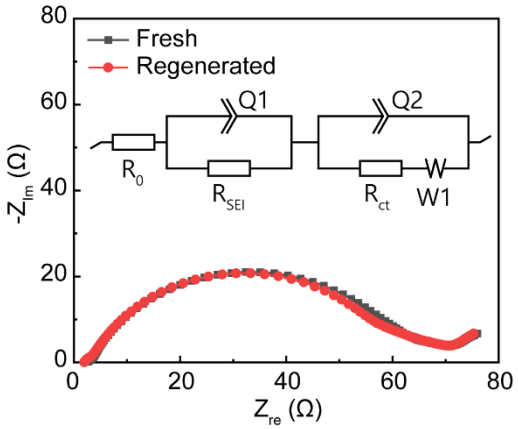

Sample name	Resistance		
	R_0 (Ω)	R_{SEI} (Ω)	R_{ct} (Ω)
Fresh	2.509	55.73	23.68
Regenerated	1.722	40.59	29.34

Fig. S12 (**a**) Nyquist plots and equivalent circuit of the half cells assembled with an NMC622 cathode before and after regeneration. The fresh and regenerated cathodes were charged to 4.3 V before the EIS analyses for a fair comparison under identical SOC. (**b**) SEI resistance (R_{SEI}) and the charge-transfer resistance (R_{ct}) of the NMC cathodes obtained by fitting the Nyquist plots.

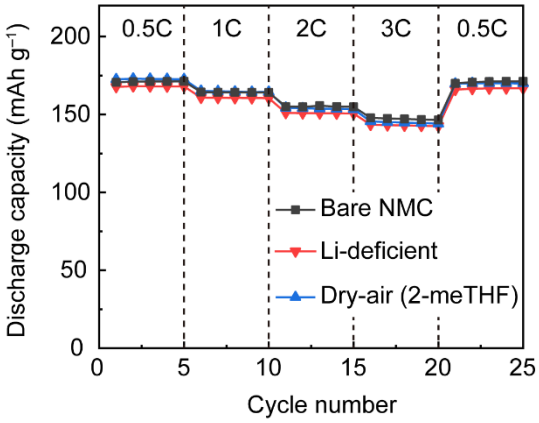

Fig. S13 The rate capability of fresh NMC622 (black), Li-deficient NMC622 (red), and NMC622 regenerated in dry-air (blue) measured in half cells after three formation cycles at 0.1C. The Li-deficient cathode was prepared by charging the cathode to 30% SOC. The regenerated NMC exhibited a high rate capability (145.6 mAh g^{-1} at 3C), similar to that of the fresh NMC (147.8 mAh g^{-1} at 3C) and Li-deficient NMC (143.5 mAh g^{-1} at 3C), indicating no side reaction during the regeneration process.

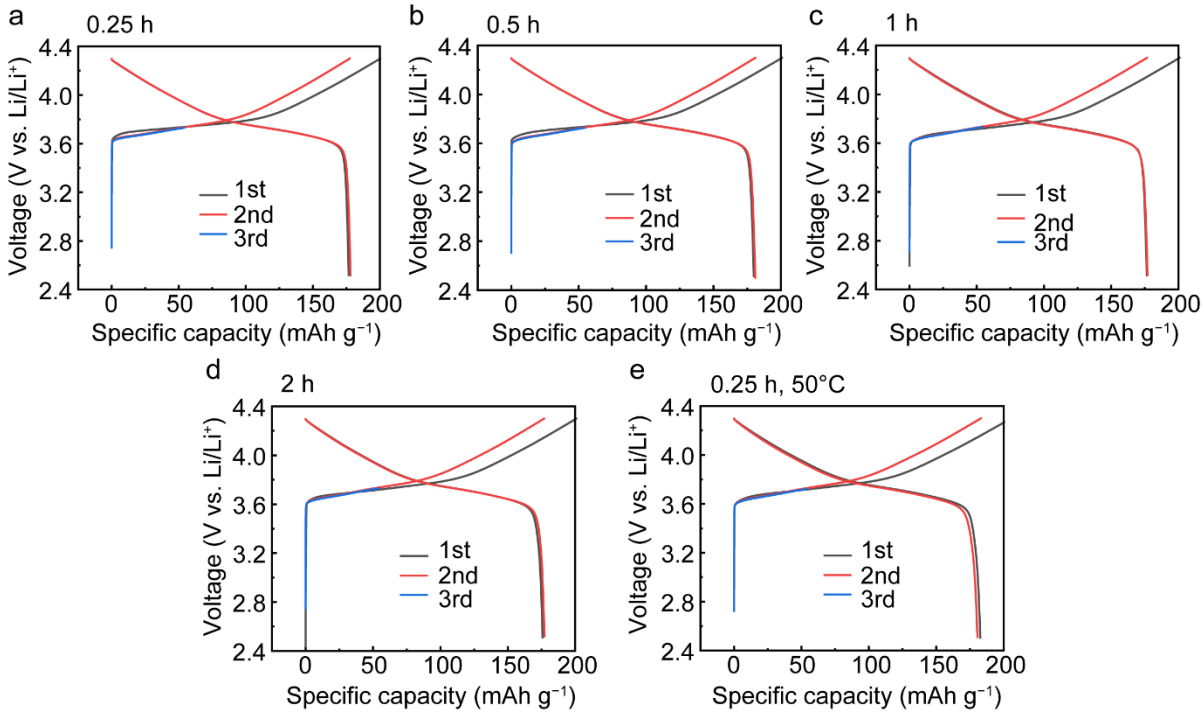

Fig. S14 Charge/discharge profiles for preparing Li-deficient NMC622 cathodes (30% SOC) for time- and temperature-dependent regeneration tests in Figure 2f. The time and temperature conditions for the regeneration are (**a**) 0.25 hour, (**b**) 0.5 hour, (**c**) 1 hour, (**d**) 2 hours, and (**e**) 0.25 hour, 50℃.

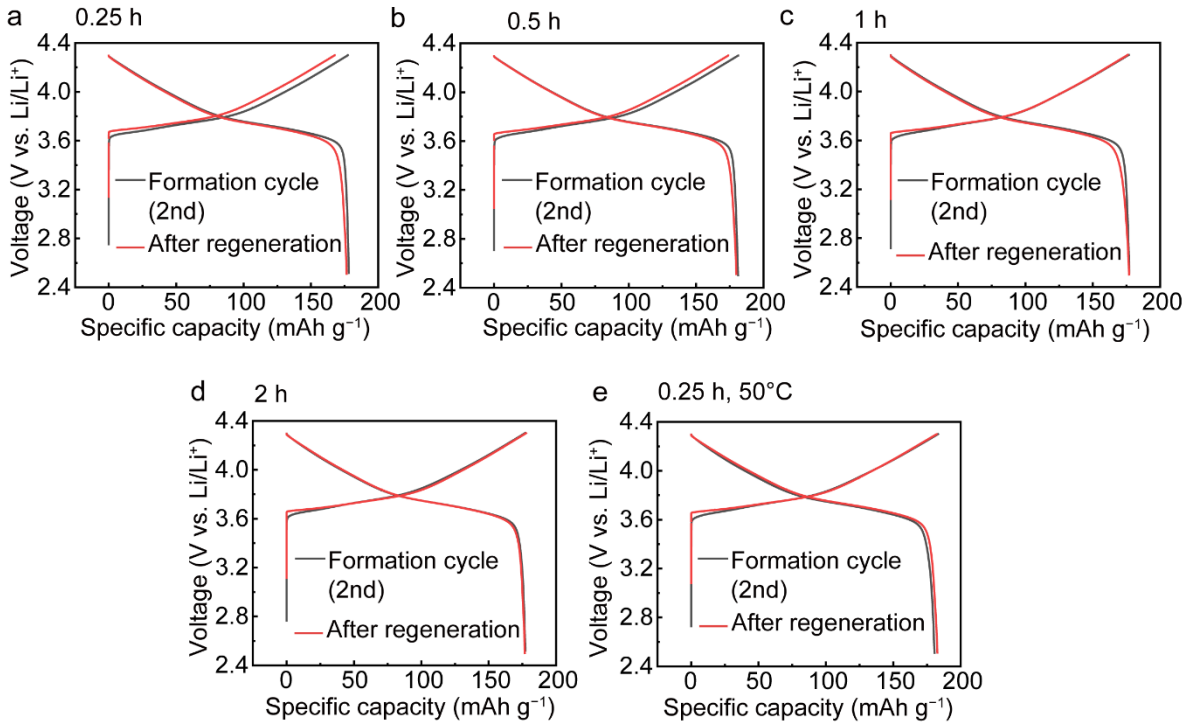

Fig. S15 Charge/discharge profiles of NMC622 cathodes before and after regeneration under the conditions in Figure 2f: (**a**) 0.25 hour, (**b**) 0.5 hour, (**c**) 1 hour, (**d**) 2 hours, and (**e**) 0.25 hour at 50 °C. Compared to formation cycle (2nd), the regenerated NMC622 cathode recovered 94.5%, 95.9%, 99.5%, 100.5%, and 99.4% of charge capacity after regeneration under 0.25 hour, 0.5 hour, 1 hour, 2 hours, (30 °C) and 0.25 hour, 50 °C conditions, respectively. The regeneration solution contained three times more DMPZ and LiTFSI than V_{Li} in NMC622.

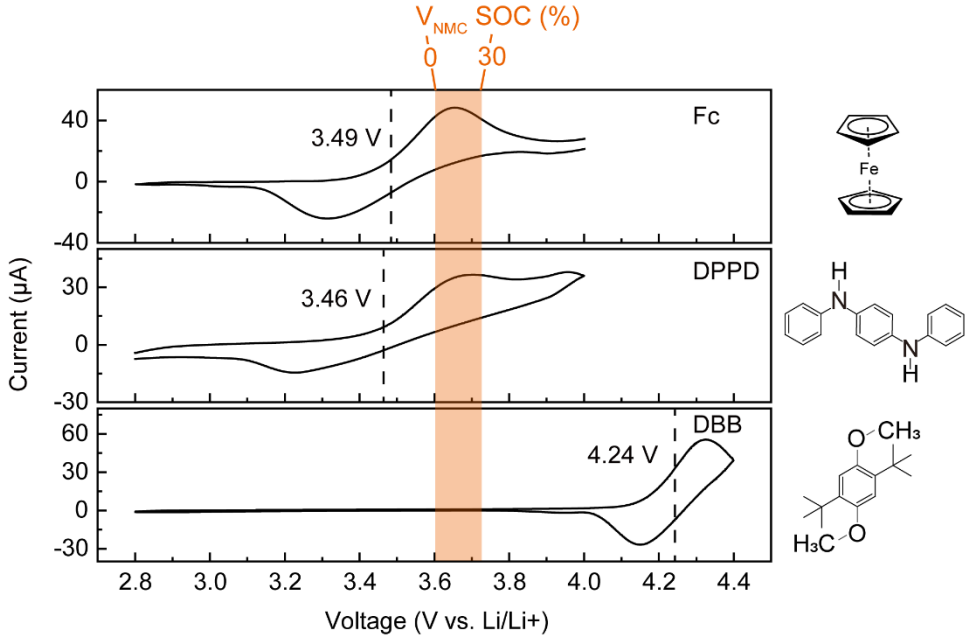

Fig. S16 Cyclic voltammograms of regeneration solutions containing RED (Fc, DPPD, or DBB) and LiTFSI at a scan rate of 1 mV s^{-1}. The Fc/Fc^+ and $DPPD/DPPD^+$ redox reactions occur at 3.49 and 3.46 V (vs. Li/Li^+), respectively, which is suitable for the chemical lithiation of Li-deficient cathodes. On the other hand, DBB exhibits much higher redox potential ($E^{DBB/DBB+}_{1/2}$ = 4.24 V vs. Li/Li^+) than the reduction potential of Li-deficient NMC (3.73 V vs. Li/Li^+).

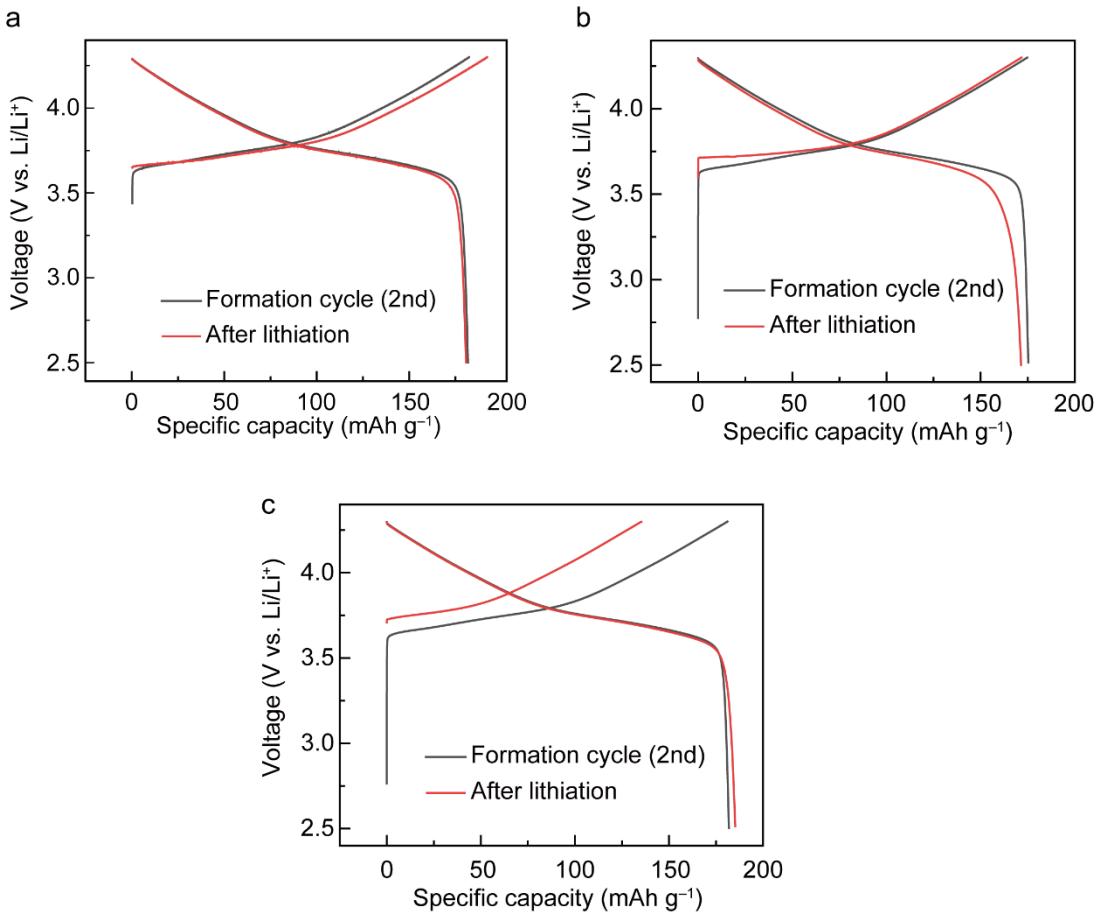

Fig. S17 Charge/discharge profiles of NMC622 cathodes after regeneration using (**a**) Fc, (**b**) DPPD, and (**c**) DBB as REDs. The cathodes were immersed in Fc-, DPPD-, and DBB-based regeneration solutions for 1 hour, 0.25 hour, and 0.25 hour, respectively. Each regeneration solution contained ten times more RED and LiTFSI than V_{Li} in NMC622, respectively. The recovered charge capacities using Fc, DPPD, and DBB were 105.3% (with a CE of 94.1%), 98.3% (with a CE of 99.8%), and 81.3% (with a CE of 125.1%), respectively, of the 2nd charge capacity of the fresh cathode.

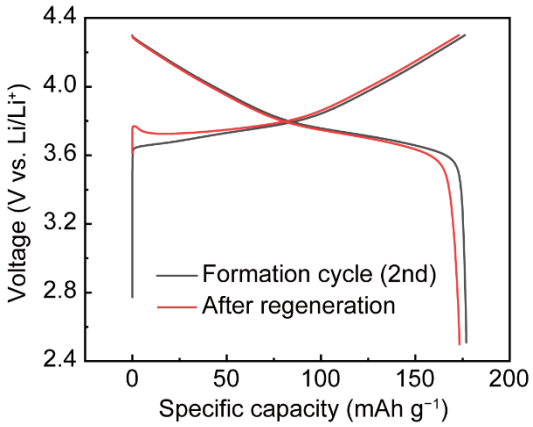

Fig. S18 Charge/discharge profiles of the NMC622 cathode before and after immersion (0.25 hour) in a regeneration solution containing ten times more DMPZ and $LiPF_6$ than V_{Li} in NMC622. The recovered charge capacity was 98.2% of that of the fresh cathode. The incomplete lithium is attributed to the instability of $LiPF_6$ to moisture and light.

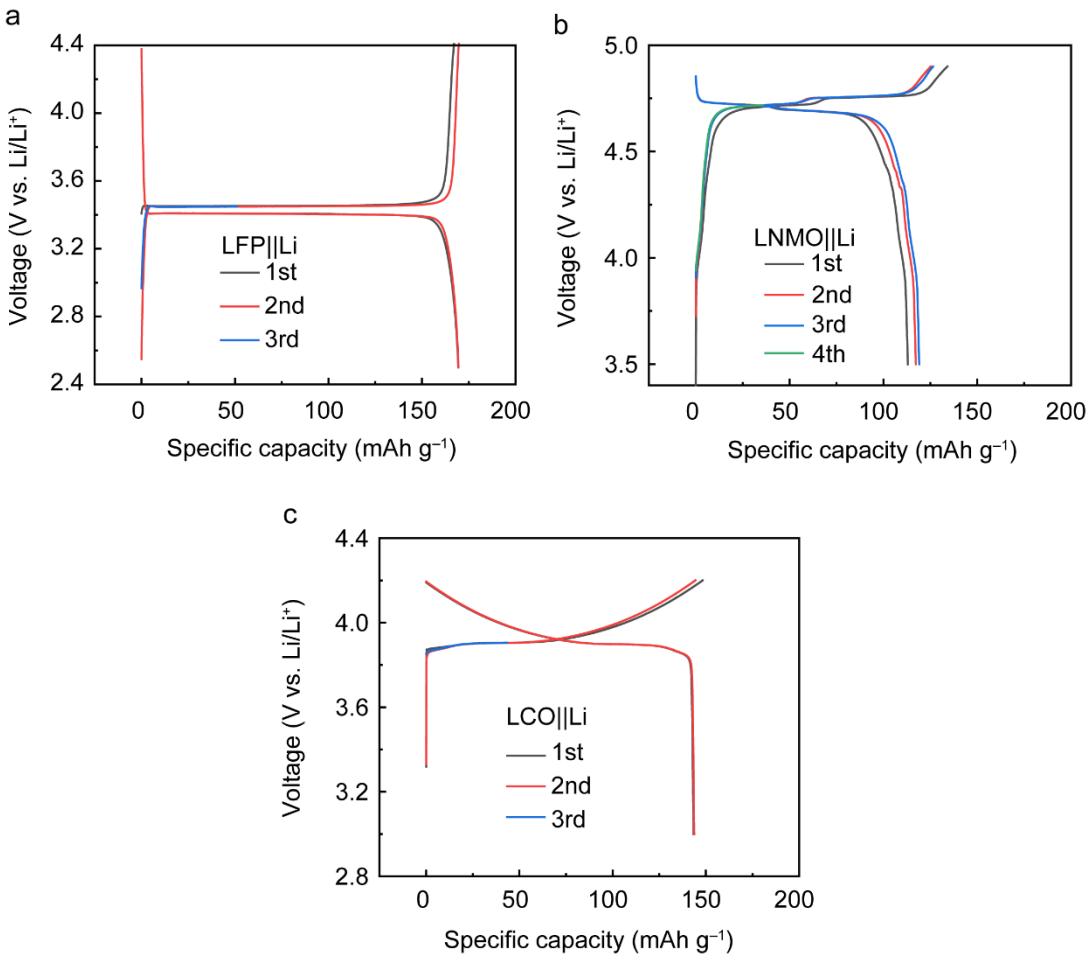

Fig. S19 Voltage profiles for preparing Li-deficient (**a**) LFP, (**b**) LNMO, and (**c**) LCO cathodes for testing the universality of the proposed regeneration method. After charging to 30% SOC (51 mAh g^{-1}, 36 mAh g^{-1}, and 43 mAh g^{-1} for LFP, LNMO, and LCO, respectively), 29.9%, 24.4%, and 15.8% V_{Li} were formed in LFP, LNMO, and LCO cathodes. The theoretical capacities of LFP, LNMO, and LCO are 170 mAh g^{-1}, 147 mAh g^{-1}, and 274 mAh g^{-1}, respectively. Each half cell using Li anode was cycled at 0.1C between the voltage range of 4.5–2.5, 4.9–3.5, and 4.3–3.0 V for LFP, LNMO, and LCO, respectively.

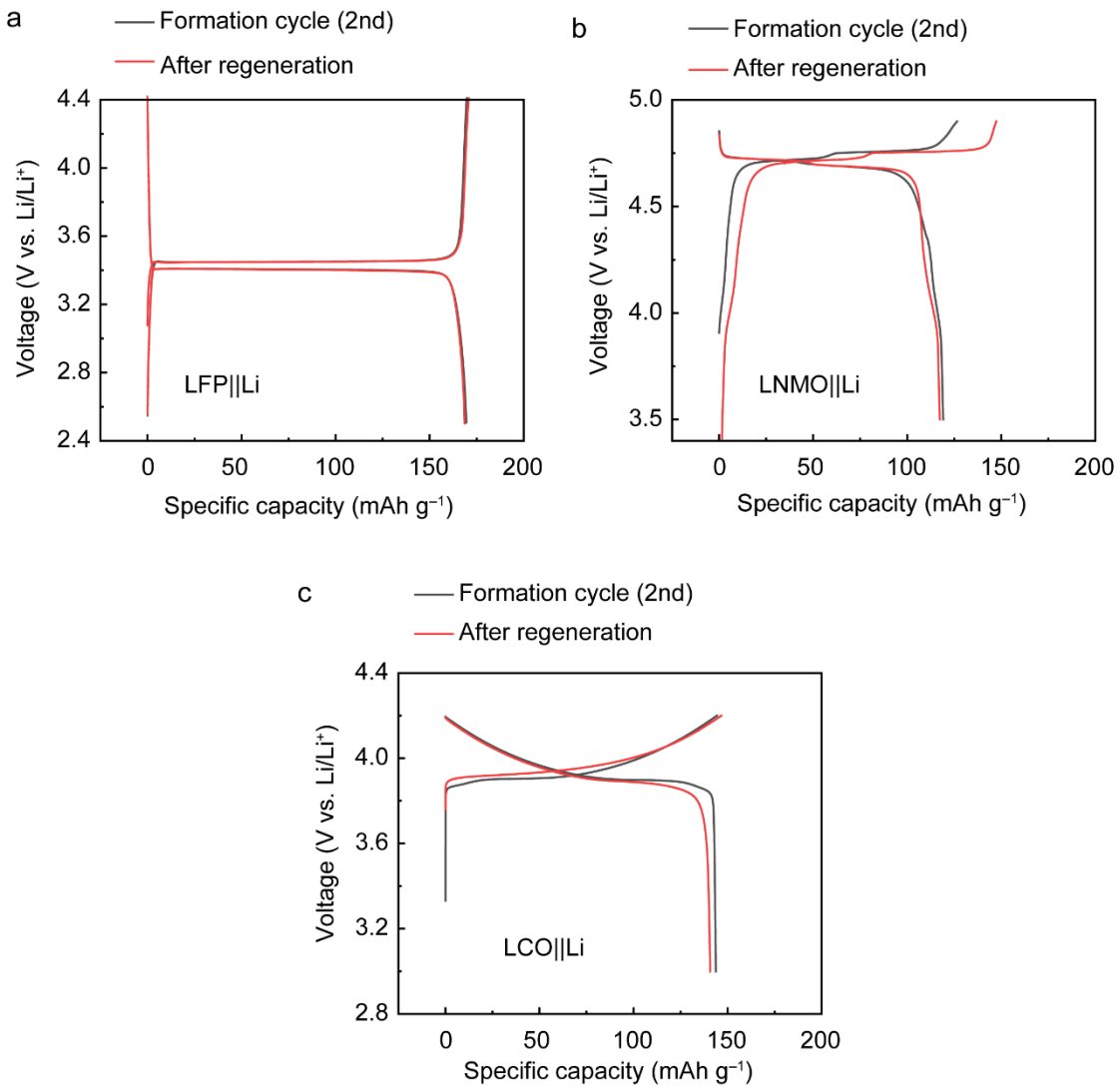

Fig. S20 Charge/discharge profiles of (**a**) LFP, (**b**) LNMO, and (**c**) LCO cathodes after immersion (0.25 hour) in regeneration solutions containing ten times more DMPZ and LiTFSI than V_{Li} in each cathode. After regeneration, the spent LFP, LNMO, and LCO cathodes recovered 102.4%, 117.6%, and 102.1% of their charge capacities compared to formation cycle (2nd), respectively. Each half cell was cycled at 0.1C between the voltage range of 4.5–2.5, 4.9–3.5, and 4.2–3.0 V for LFP, LNMO, and LCO, respectively.

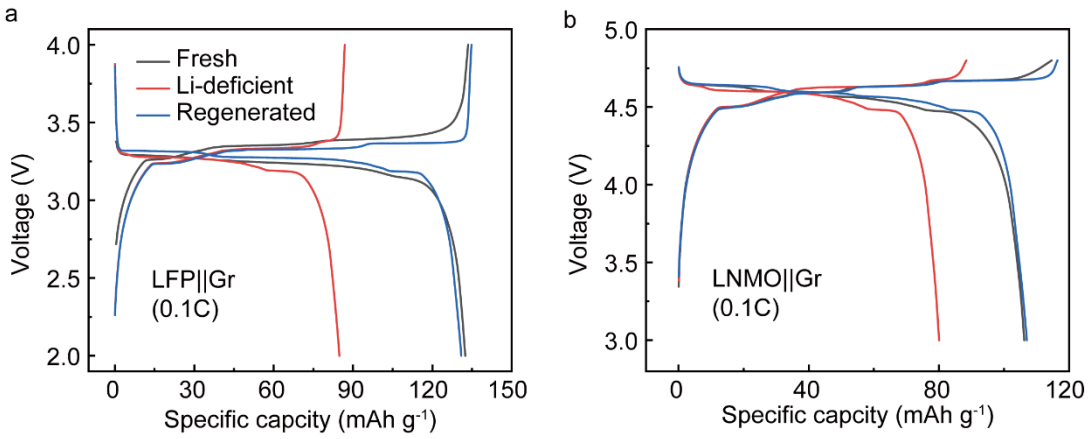

Fig. S21 Charge/discharge profiles of (**a**) LFP and (**b**) LNMO full cells paired with fresh graphite (Gr) anodes. The regenerated cathodes were prepared by immersing 30% charged electrode into the RED solution with ten times excess Li compared to V_{Li} for 2 hours at 30 °C. The full cells of the regenerated LFP and LNMO cathodes exhibited 99.2% and 100.9% of the discharge capacities compared to the full cells containing the fresh cathodes. In contrast, the full cells of Li-deficient cathodes only delivered 64.4% and 75.5% of the original discharge capacities. The C-rate was 0.1C, and the voltage ranges were 4.0–2.0 V and 4.8–3.0 V for LFP and LNMO, respectively.

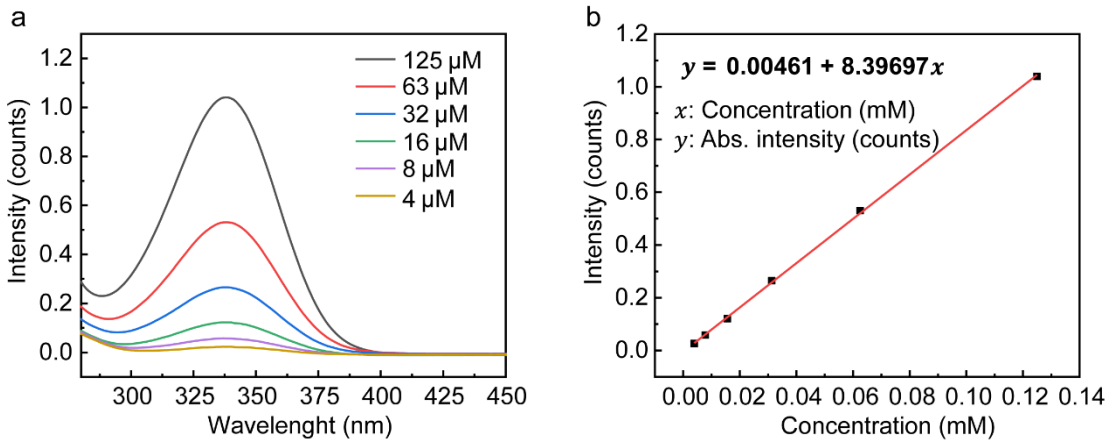

Fig. S22 (**a**) UV–vis absorption spectra of DME solutions with various DMPZ concentrations and (**b**) the standard calibration curve of absorbance intensity as a function of DMPZ concentration. The calibration points of DME-based DMPZ solutions were linearly fitted with a slope of 8.39, resulting in a correlation coefficient (R^2= 0.99) close to the ideal value, 1.

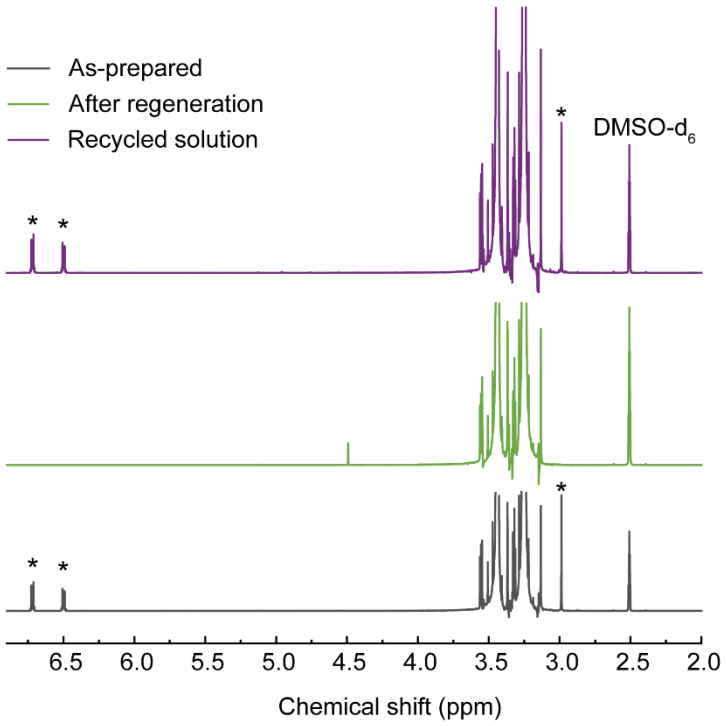

Fig. S23 1H-NMR full spectrum (6.9–2 ppm) of DMPZ solutions during the closed-loop recycling process. The characteristic peaks of DMPZ are labeled with asterisks (*).

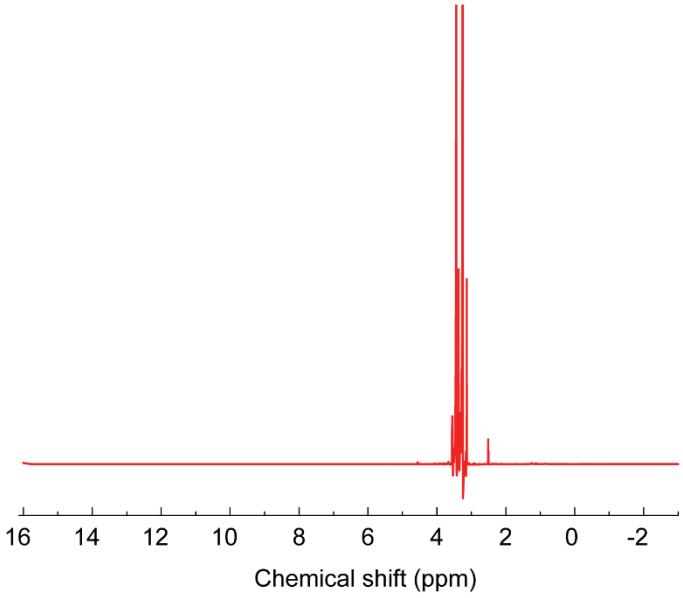

Fig. S24 1H-NMR spectrum of the DME solution containing only LiTFSI (22.5 mmol L^{-1}).

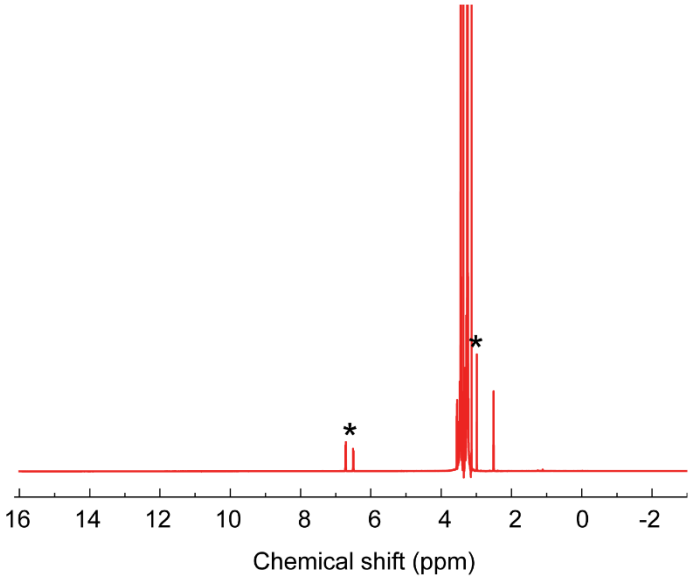

Fig. S25 1H-NMR spectrum of the regeneration solution containing DMPZ (21 mmol L^{-1}) and LiTFSI (22.5 mmol L^{-1}). The characteristic peaks of DMPZ are labeled with asterisks (*).

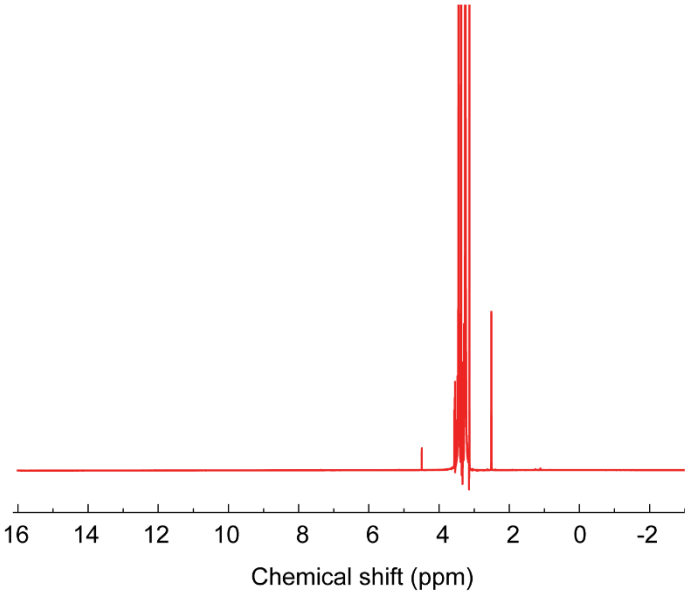

Fig. S26 1H-NMR spectrum of the regeneration solution (from Supplementary Figure S21) after processing Li-deficient NMC622 for 2 h.

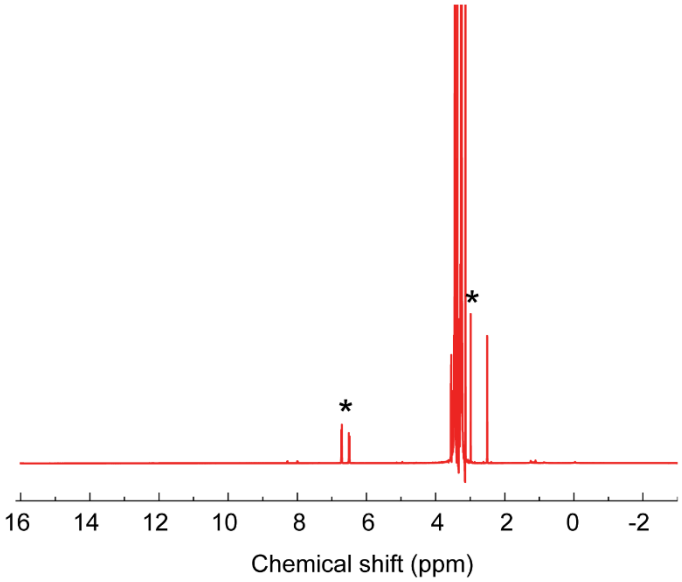

Fig. S27 1H-NMR spectrum of the used regeneration solution (from Supplementary Figure S22) after mixing with 1.9 mmol of Li_2O_2. The characteristic peaks of DMPZ are labeled with asterisks (*).

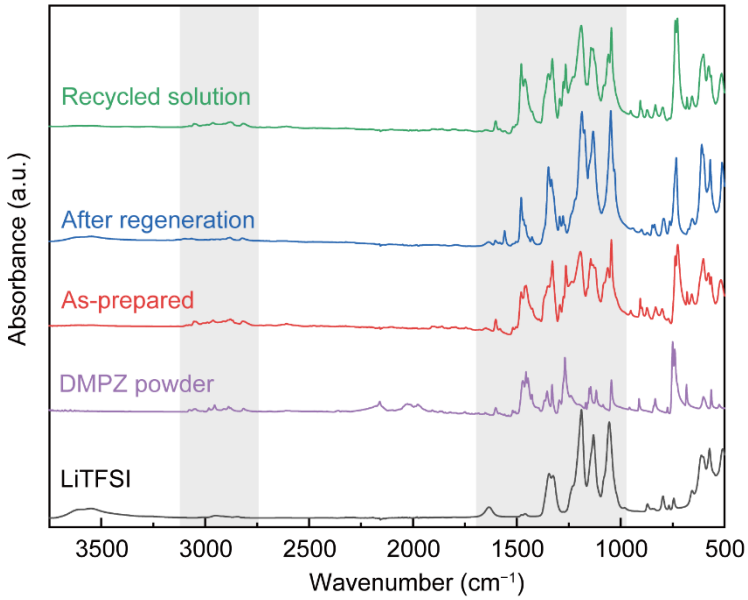

Fig. S28 Full range FT-IR spectra of DMPZ solution during the closed-loop recycling process. The grey-shaded areas in the FT-IR spectra represent characteristic peaks of DMPZ.

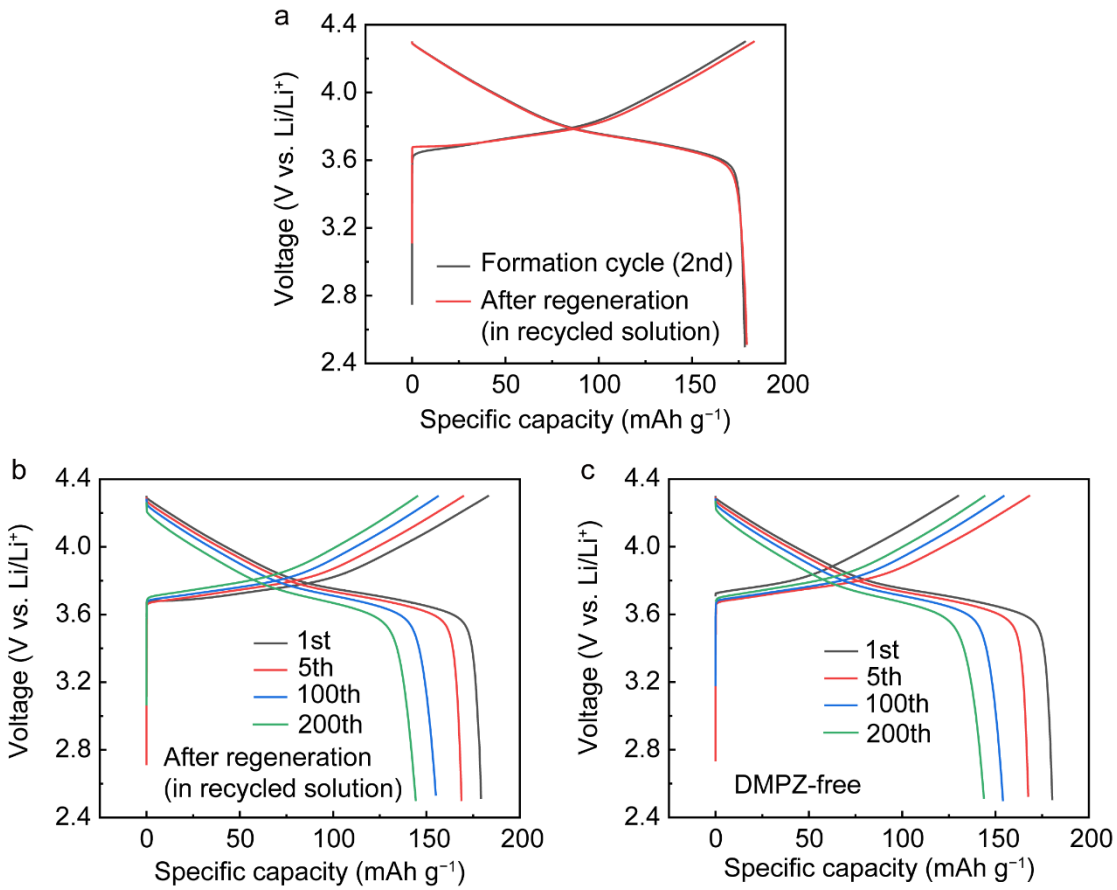

Fig. S29 (**a**) Charge/discharge profiles of the Li-deficient NMC622 cathodes in half cells before and after regeneration in the recycled DMPZ solution. Long-term cyclability of NMC622 cathode treated in (**b**) recycled DMPZ solution and (**c**) DMPZ-free solution. The regenerated NMC622 cathode exhibited negligible differences in overpotentials during cycling, retaining 85.3% of its reversible capacity over 200 cycles.

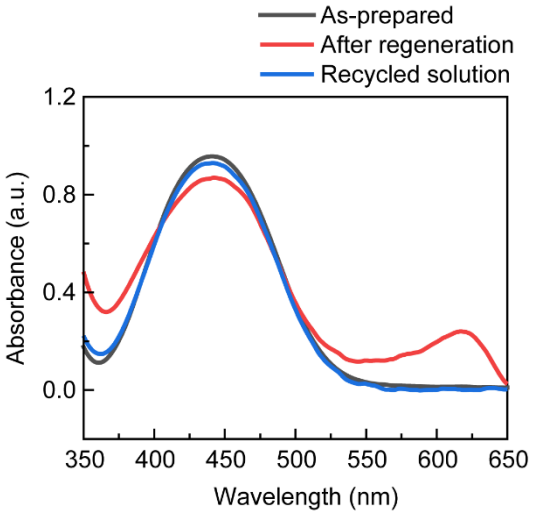

Fig. S30 UV–vis absorption spectra of Fc solution during the closed-loop recycling process using Li_2S as reducing agent. The characteristic peak of Fc^+ (619 nm) completely disappeared, and the peak from Fc^0 at 441 nm recovered its original intensity after mixing with Li_2S, confirming the high-yield conversion of Fc^+ to Fc^0. The molar ratio of Li_2S: Fc was 0.6 (Li: RED = 1.2).

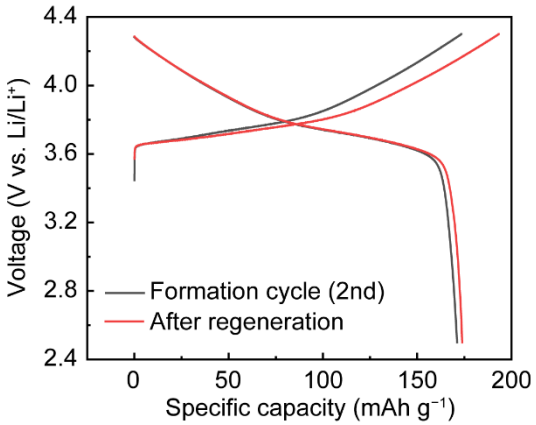

Fig. S31 Charge/discharge profiles of the NMC622 cathode before and after regeneration in the reused Fc-based RED solution after treating with Li_2S. The regeneration solution contained ten times more Fc and LiTFSI than V_{Li} in Li-deficient NMC622.

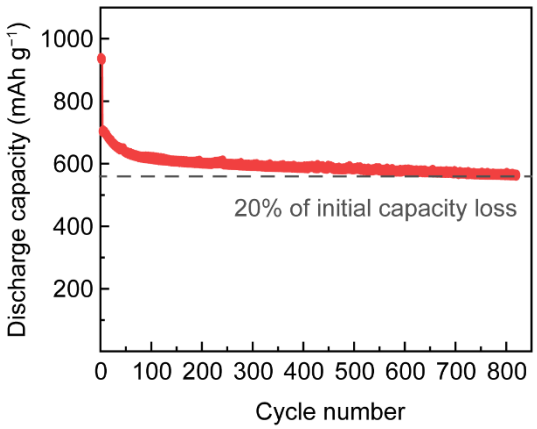

Fig. S32 The capacity retention of a commercial 1-Ah-capacity pouch cell cycled at 1C for 820 cycles after three initial cycles at 0.1C. The pouch cell exhibited a 20% loss in discharge capacity after 823 cycles.

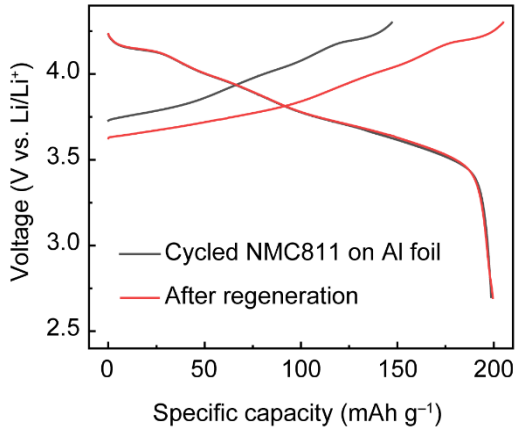

Fig. S33 The charge/discharge profile of the cycled and regenerated NMC811 cathode from the 20% degraded 1-Ah pouch cell. The 'cycled NMC811 on Al foil' represents the retrieved cathode from the degraded pouch cell. The voltage profile was obtained from a half cell by pairing the spent cathode with a Li metal anode. While the cycled NMC811 showed an initial charge capacity of 147.1 mAh g^{-1} due to the Li loss in the cathode crystal structure, the regenerated NMC811 exhibited an initial charge capacity of 204.9 mAh g^{-1} with CE of 97.3%. The voltage range was 4.3–2.5 V, and the C-rate was 0.1C (= 20 mA g^{-1}).

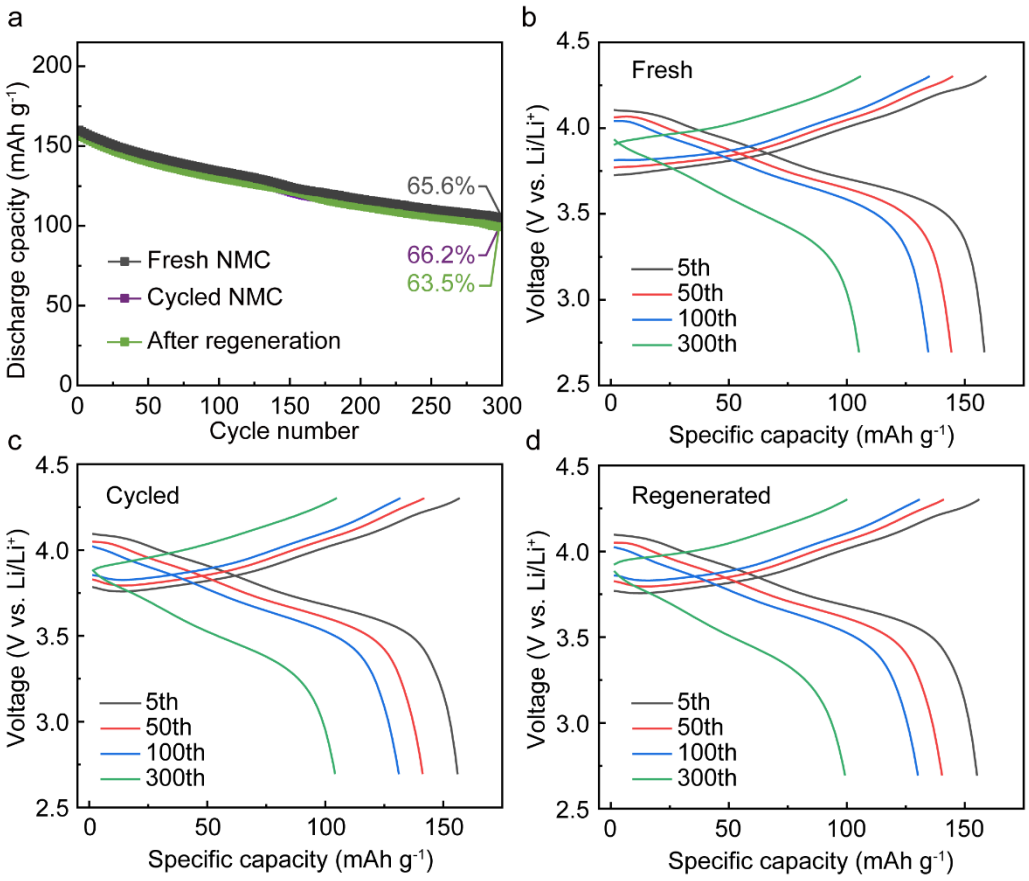

Fig. S34 (**a**) The long-term cyclability of NMC811||Li half cells assembled with NMC811 cathodes in different states (fresh, cycled, and regenerated) at 3C. The cycled NMC811 cathodes were retrieved from the pouch cell with 60% capacity loss and chemically lithiated in the regeneration solution containing DMPZ and LiTFSI. Charge/discharge profiles for the 5th, 50th, 100th, and 300th cycles during long-term cycling (3C) of (**b**) fresh, (**c**) cycled, and (**d**) regenerated NMC811 cathodes. The regenerated NMC cathode exhibited comparable capacity retention and voltage profiles with other cathodes, demonstrating that the regeneration process does not compromise the integrity of the active cathode particles, even under real long-term cycling.

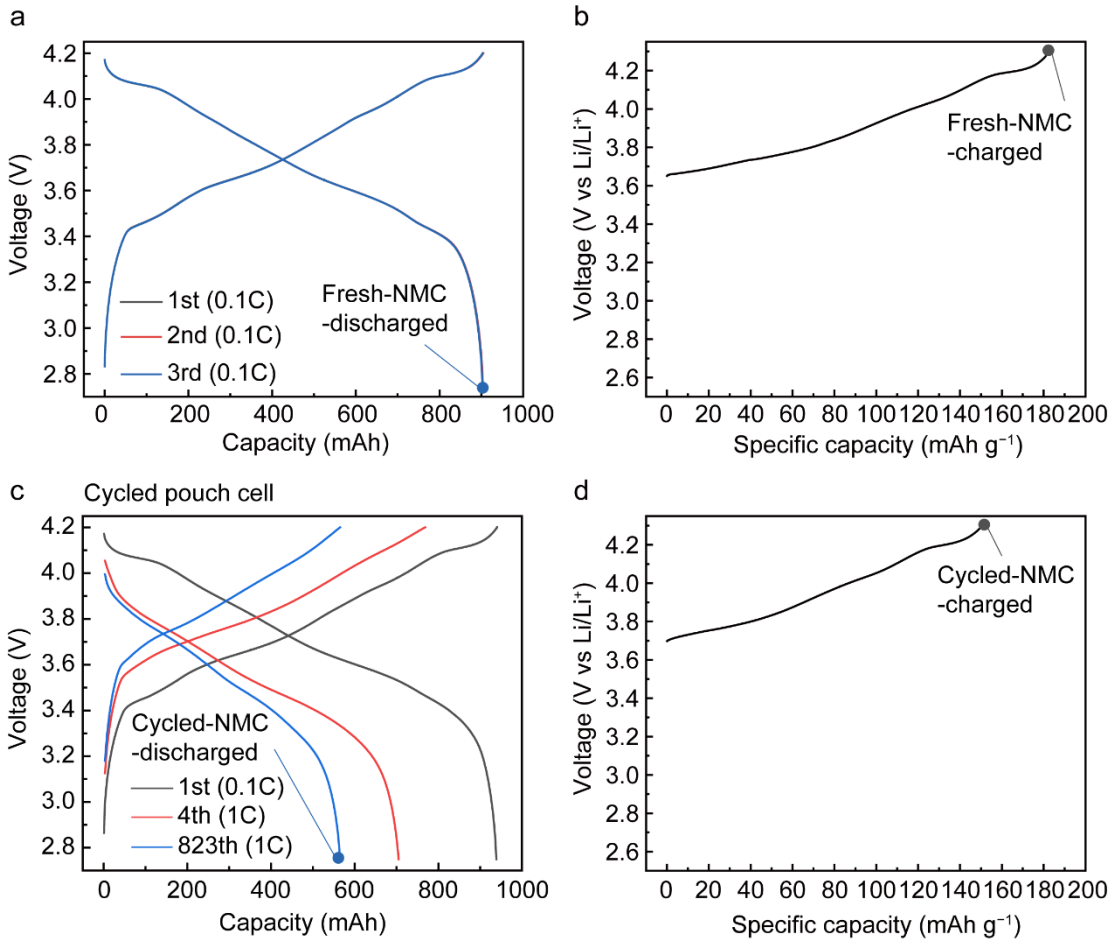

Fig. S35 (**a**) Charge/discharge profiles of a commercial 1-Ah-capacity pouch cell for initial three cycles after formation. After harvesting discharged NMC811 cathode (denoted as "f-NMC-d") from (a) and reassembling it into a half cell, (**b**) the cell was fully charged to 4.3 V (vs. Li/Li^+) and the cathode was retrieved (denoted as "f-NMC-c"). (**c**) After 823 cycles, the discharged cathode ("c-NMC-d") was retrieved and (**d**) reassembled in a half cell to obtain the charged cathode "c-NMC-c".

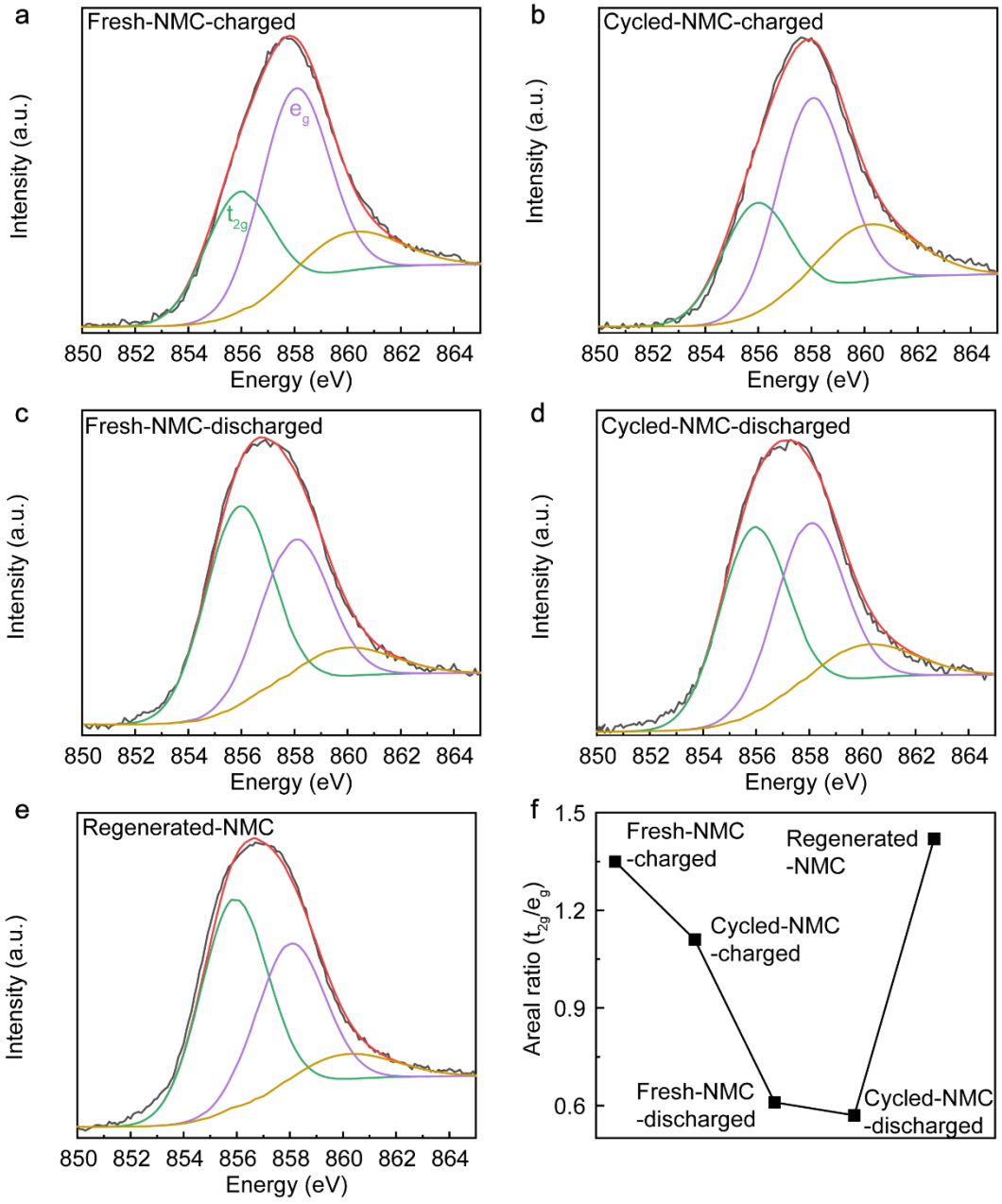

Fig. S36 (**a–e**) Gaussian deconvolution of the peaks from t_{2g} and e_g levels in the Ni L-edge NEXAFS FY mode spectra of NMC811 cathodes at different electrochemical and regeneration states. The NEXAFS spectra was deconvoluted into two peaks centered at 856 eV and 858 eV with the same full width at half-maximum (FWHM) of 3 eV. (**f**) The t_{2g}/e_g areal ratio of the NMC811 cathode decreased with increasing V_{Li} in NMC811. After regeneration (r-NMC), the areal ratio recovered close to the fresh NMC811 cathode in the discharged state (f-NMC-d).

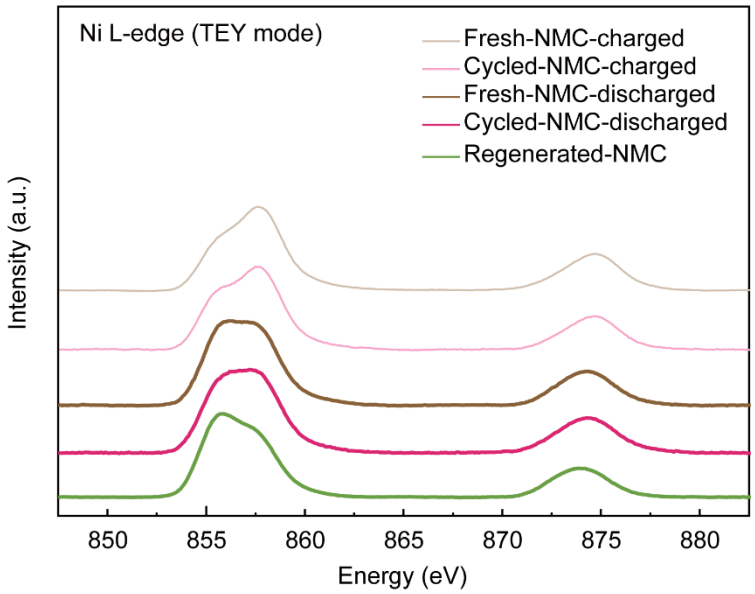

Fig. S37 The Ni L-edge NEXAFS TEY mode spectra of NMC811 cathodes at different electrochemical and regeneration states. With fewer V_{Li} in NMC, the more L_3 and L_2 peaks shifted toward lower energy, indicating the decreased concentration of high-valence Ni ions in the cathode crystal structure.

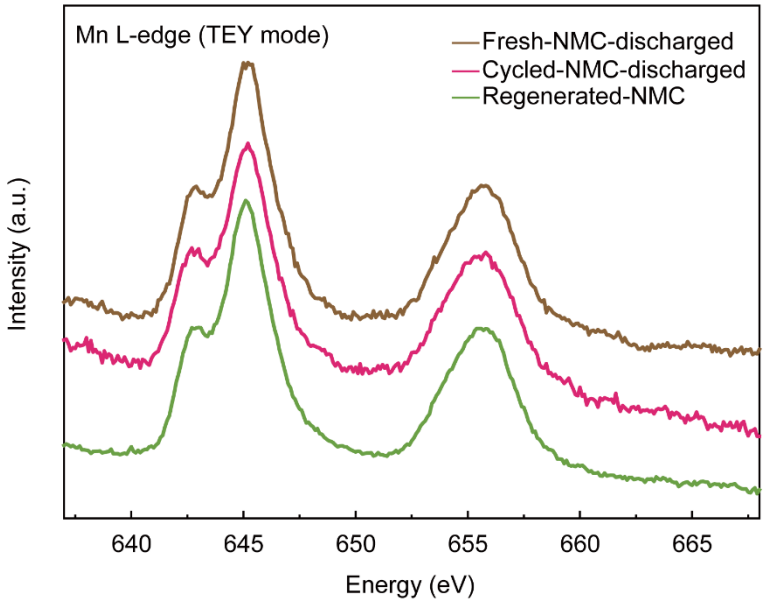

Fig. S38 The Mn L-edge NEXAFS TEY mode spectra of NMC811 cathodes at different electrochemical and regeneration states. All samples exhibited Mn^{4+} dominant spectra, confirming that the layered crystal structure of NMC811 was well maintained on the surface region during the cycling or regeneration process.

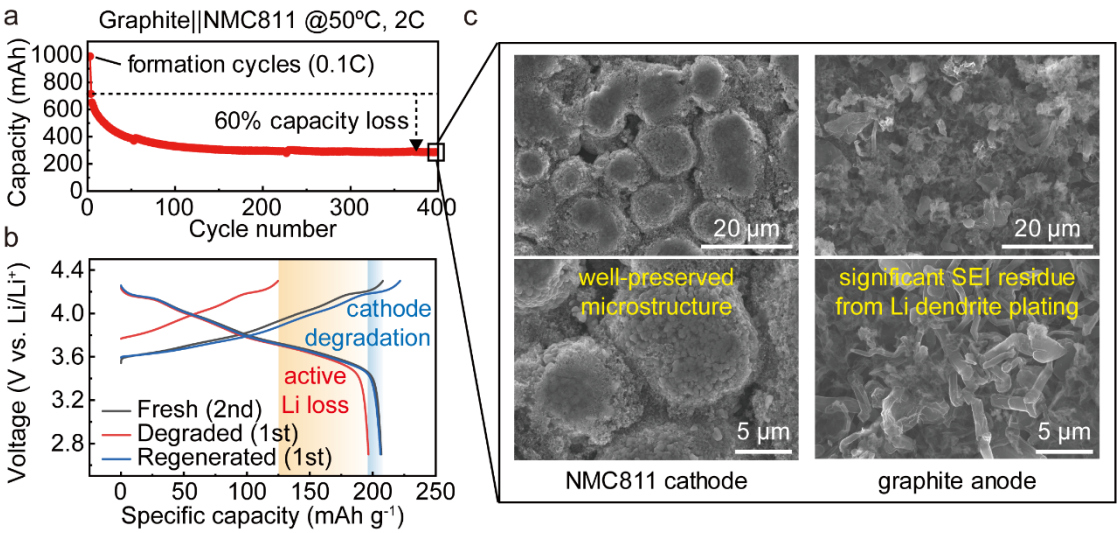

Fig. S39 (**a**) The capacity retention of a NMC811||graphite 1 Ah-sized pouch cell at 50 °C, which showed 60% capacity loss after 400 cycles. (**b**) Voltage profiles of fresh NMC811, degraded NMC811 from (a), and regenerated NMC811. The profiles were obtained using half cells with Li metal anodes. The reduced initial charge capacity of the degraded sample clearly indicates the limited Li inventory in the spent cathode. Upon discharge, electrochemical relithiation to the degraded cathode by the unlimited Li source resulted in a discharge capacity, corresponding to nearly 95% of the original capacity from the fresh cathode. After the chemical regeneration, the cathode exhibited an initial charge capacity of 222 mAh g^{-1}, reflecting successful recovery of the original Li inventory. (**c**) SEM images showing the top surface of the cathode and anode from the cycled pouch cell in (a).

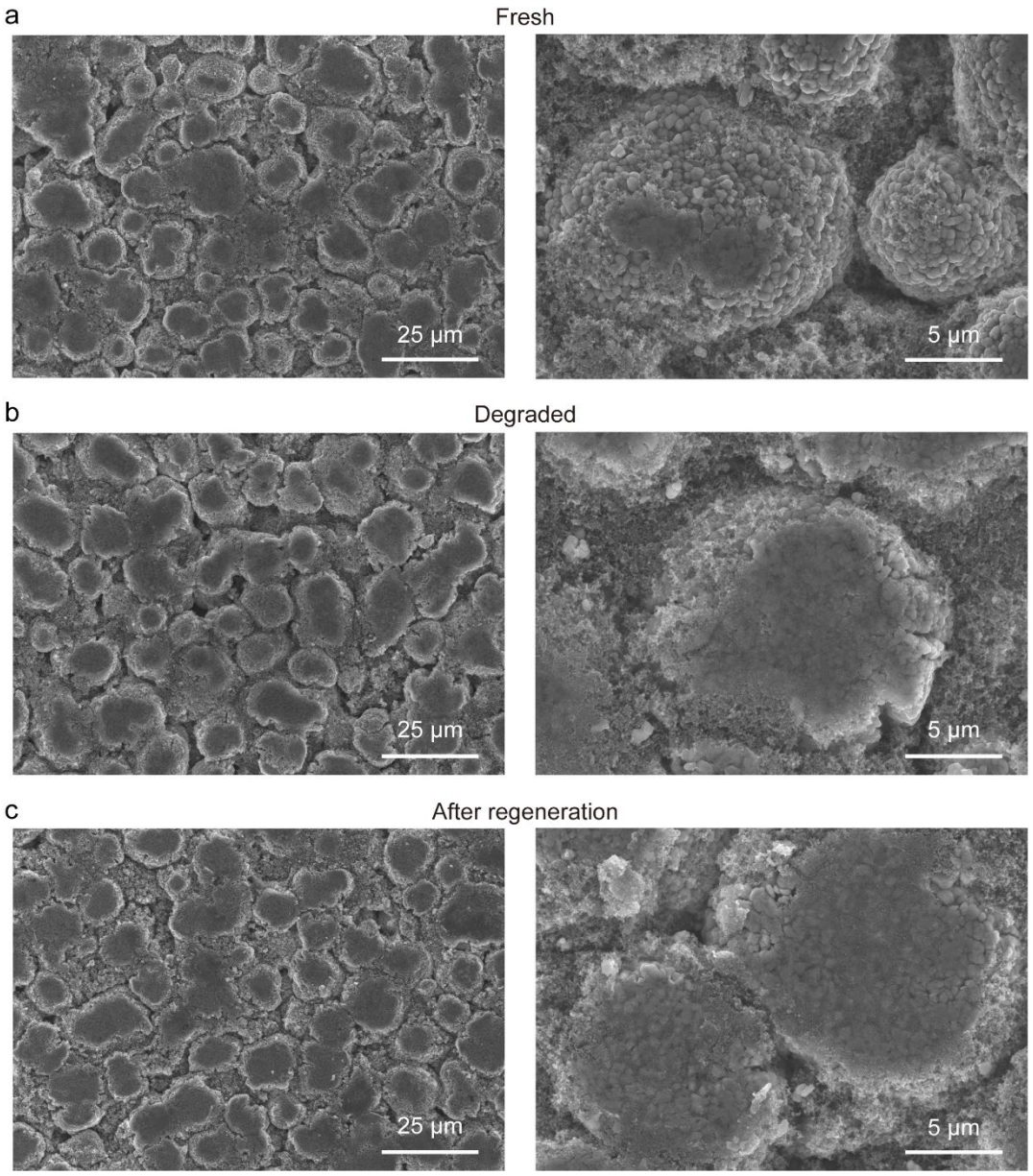

Fig. S40 SEM images of (**a**) the fresh, (**b**) degraded, and (**c**) regenerated NMC811. The degraded cathode was retrieved from an NMC811||graphite 1 Ah pouch cell with a 60% capacity loss. The subsequent cathode regeneration was conducted using the RED-based solution for 0.25 hour. The RED-based chemical lithiation preserves the cathode morphology without significant pulverization or intergranular cracking of the active particles.

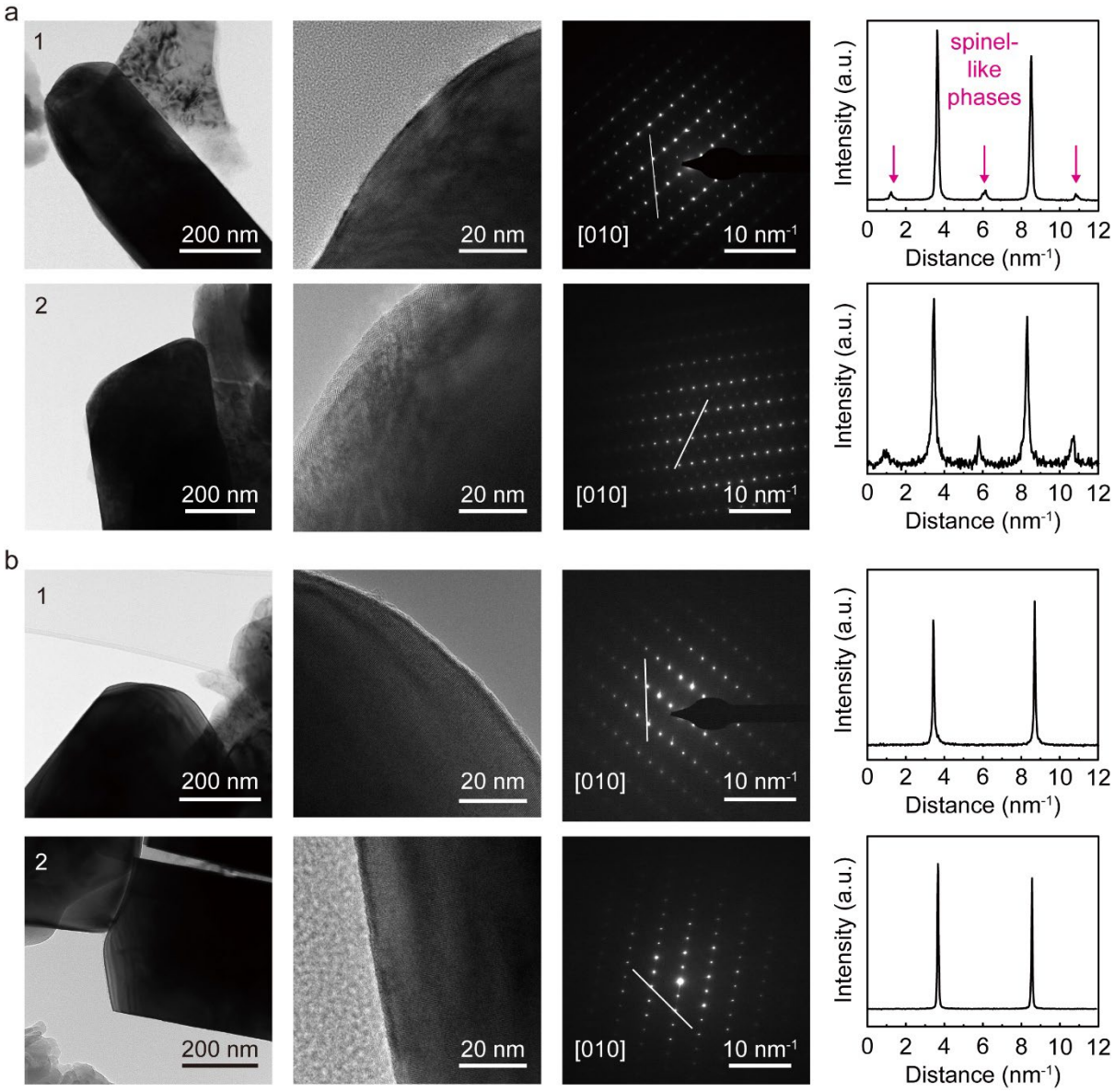

Fig. S41 TEM images and selected-area electron diffraction (SAED) patterns, accompanied by intensity histograms of the dotted lines, of cycled NMC811 from the spent battery of a 60% capacity loss (**a**) before and (**b**) after regeneration using the RED-based solution. Diffraction spots from spinel-like cation-disordered phases at the particle surface completely disappeared after regeneration.

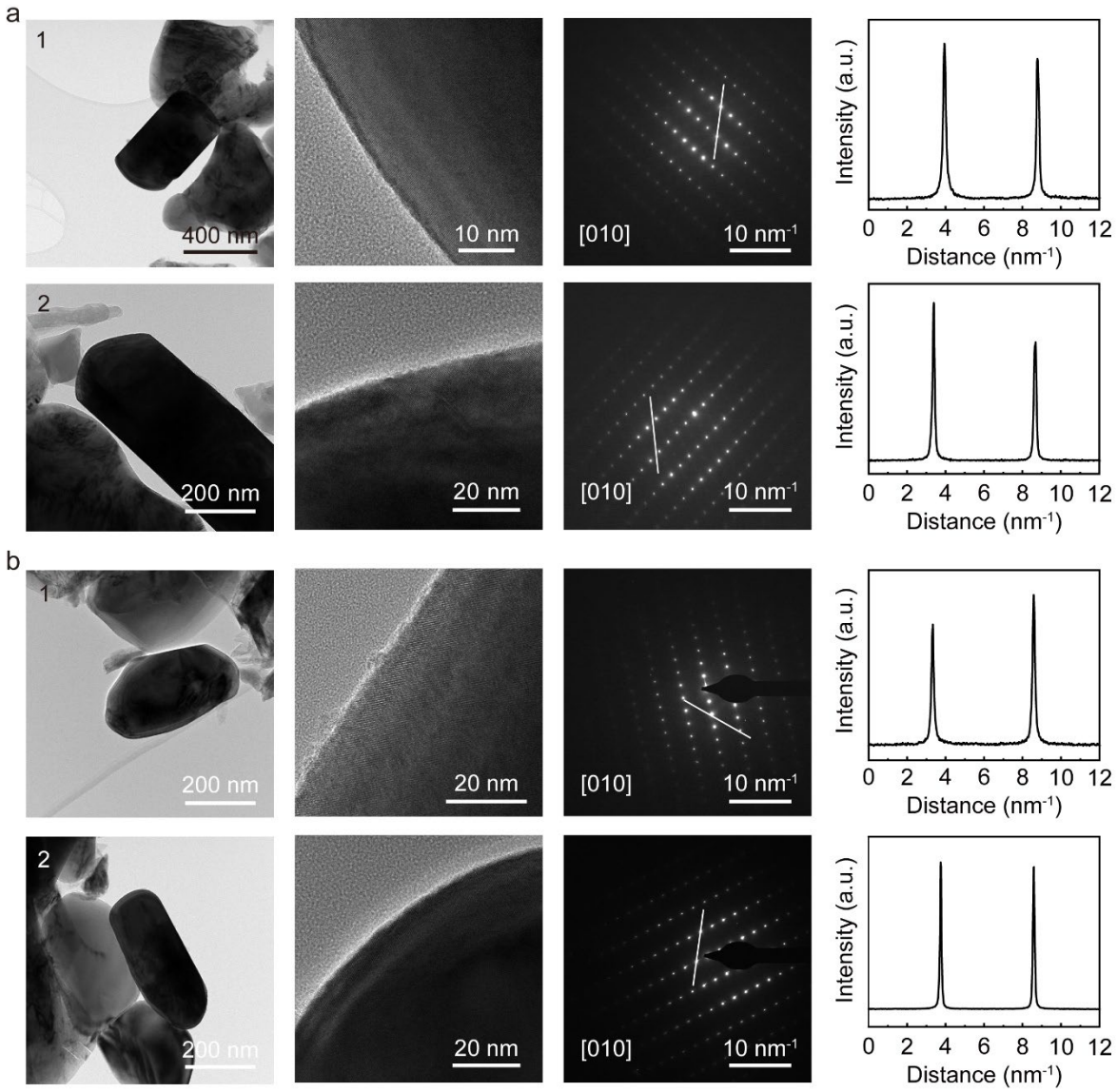

Fig. S42 TEM images and SAED patterns with intensity histograms of the dotted lines of cycled NMC811 from the spent battery of a 20% capacity loss (**a**) before and (**b**) after regeneration using the RED-based solution. The dim diffraction spots from spinel-like cation-disordered phases at the particle surface completely disappeared after regeneration.

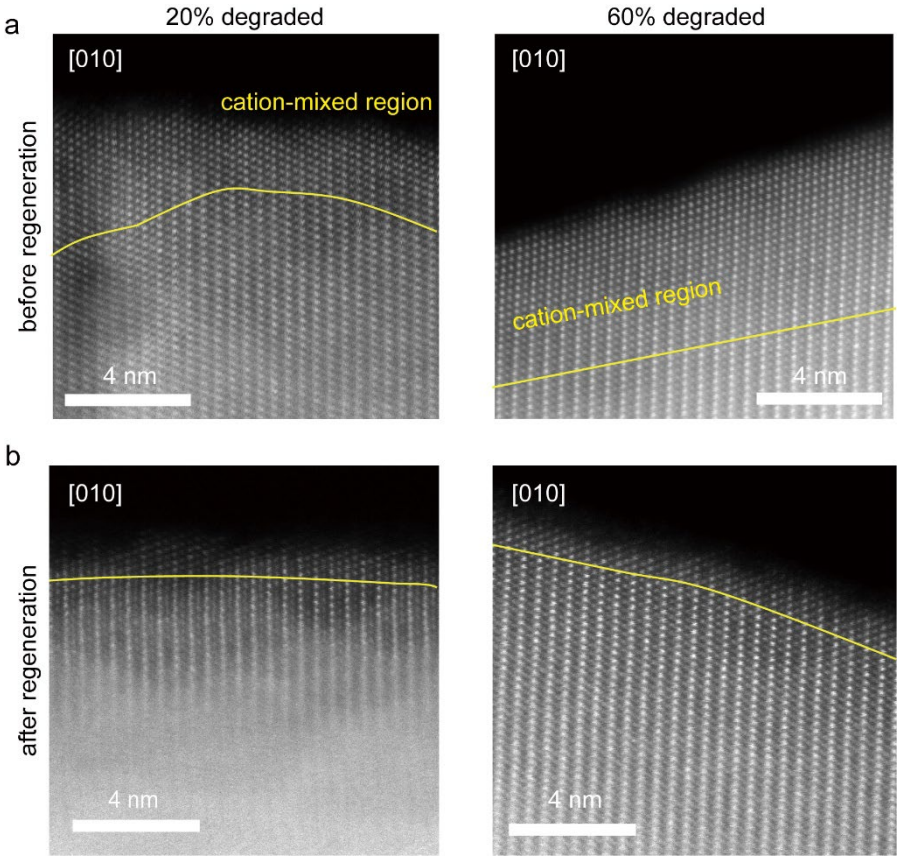

Fig. S43 Scanning transmission electron microscopy (STEM)-high angle annular dark field (HAADF) images of cycled NMC811 from the spent battery (NMC811||graphite pouch cell) with 20% (left) and 60% capacity losses (right) (**a**) before and (**b**) after regeneration using the RED-based solution. The thickness of the cation-disordered region, including rocksalt and spinel-like phases, decreased after chemical lithiation in the regeneration solution.

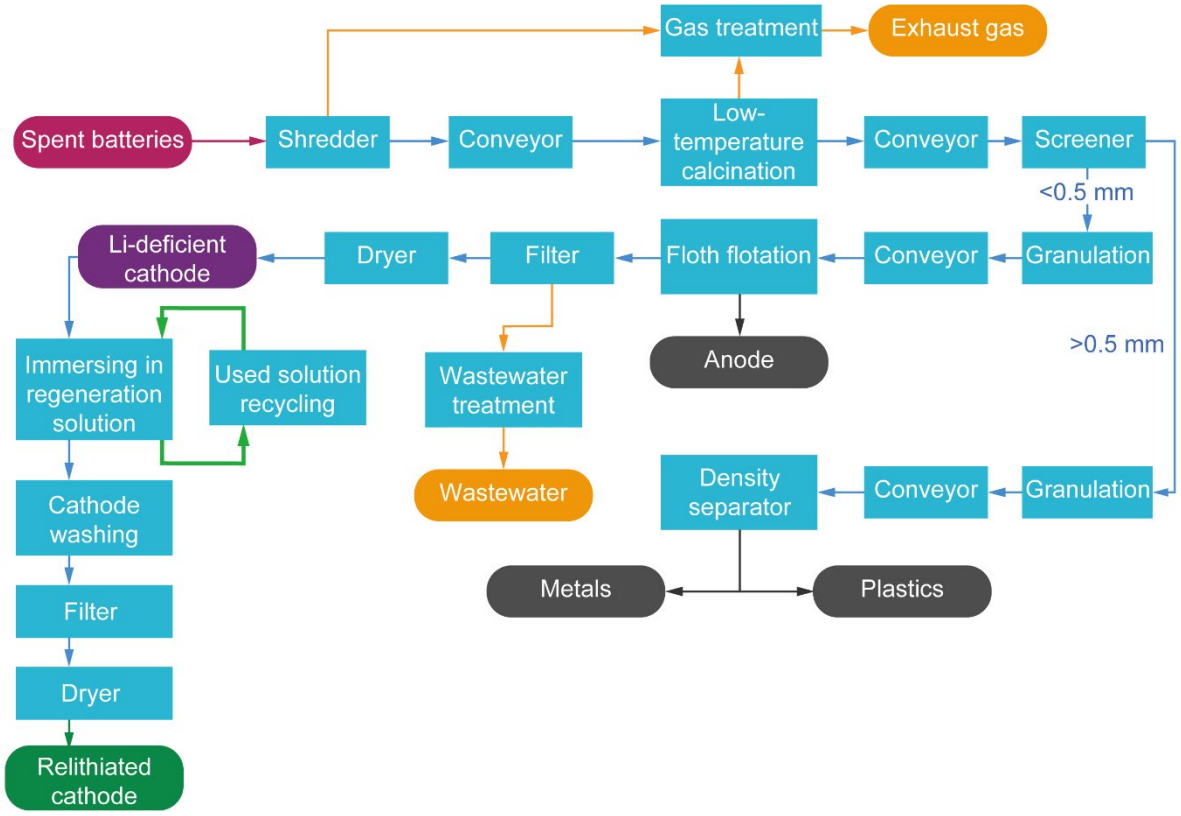

Fig. S44 A process diagram of our RED-based cathode regeneration process.

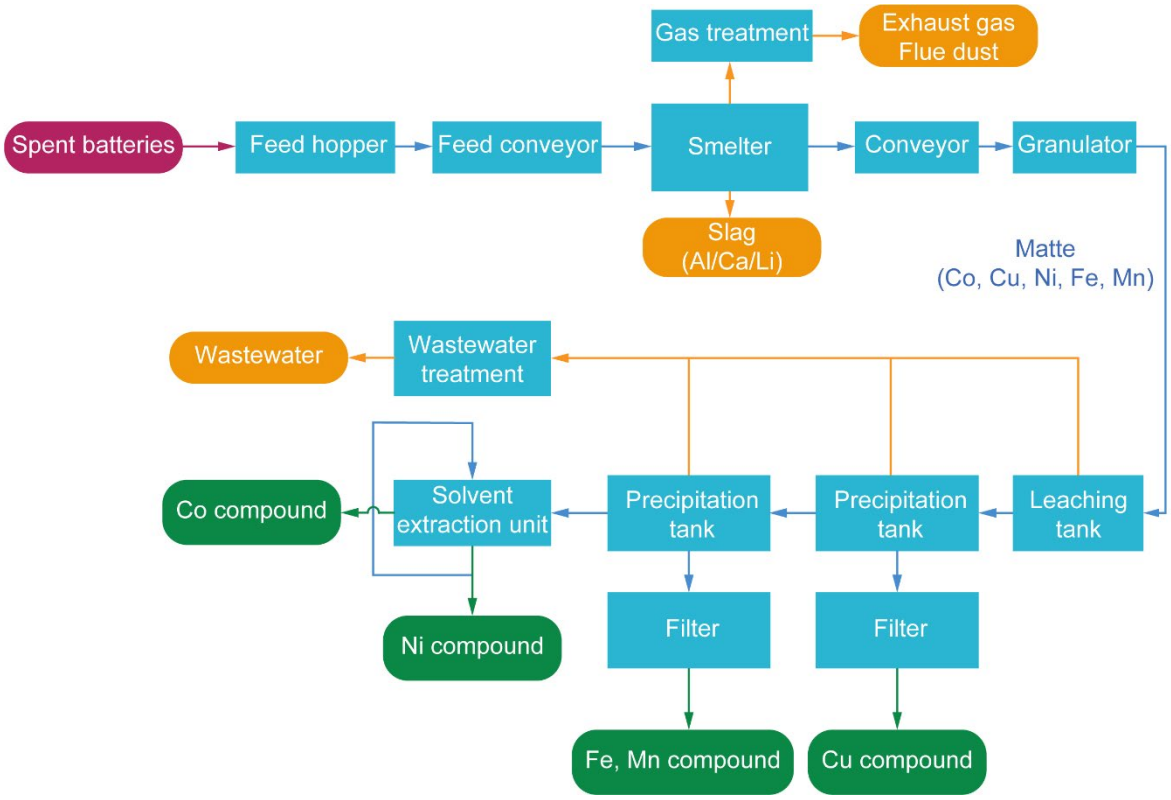

Fig. S45 A process diagram of a generic pyrometallurgical recycling process.

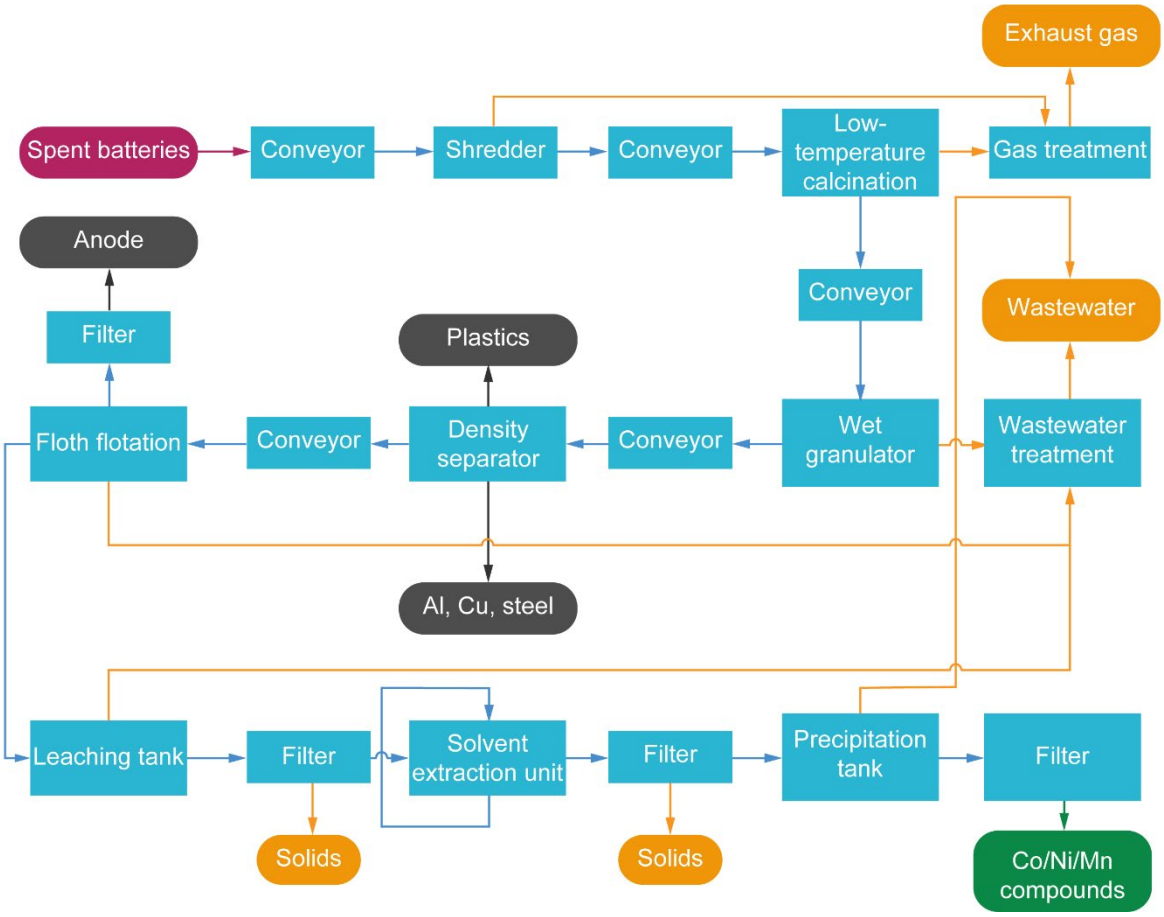

Fig. S46 A process diagram of a generic hydrometallurgical recycling process.

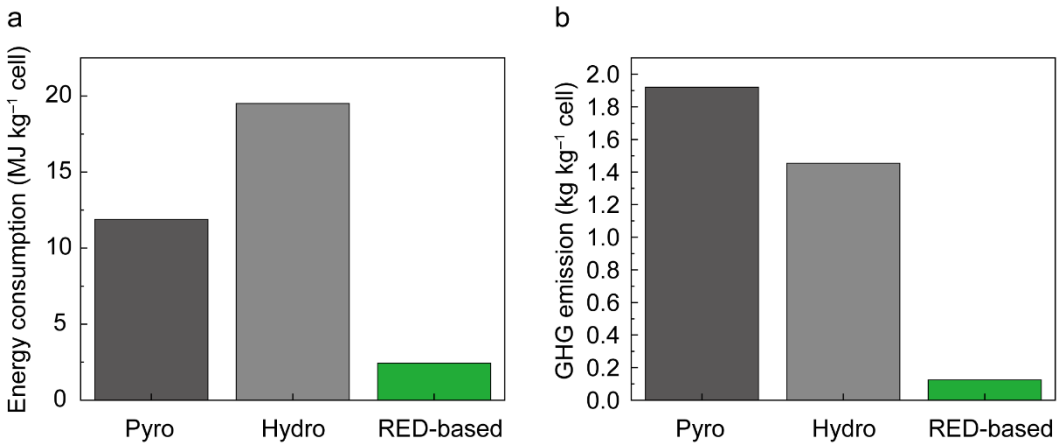

Fig. S47 (**a**) Total energy consumption and (**b**) greenhouse gas (GHG) emissions for recycling 1 kg spent battery cells with pyrometallurgical (pyro), hydrometallurgical (hydro), and RED-based processes.

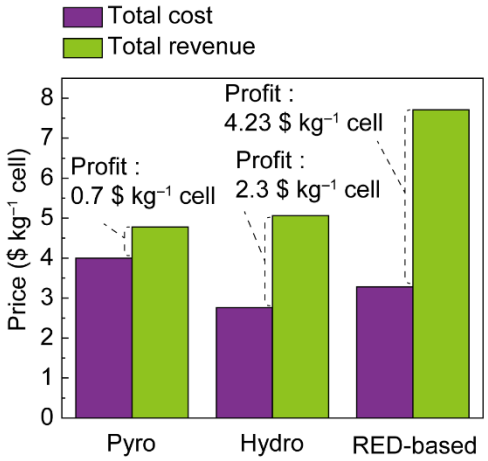

Fig. S48 Cost and revenue per kg of spent battery cells recycled by pyrometallurgical (pyro), hydrometallurgical (hydro), and RED-based processes. The profits of recycling 1 kg of spent battery cells are USD 0.7, 2.3, and 4.2 for pyro, hydro, and RED-based methods, respectively.

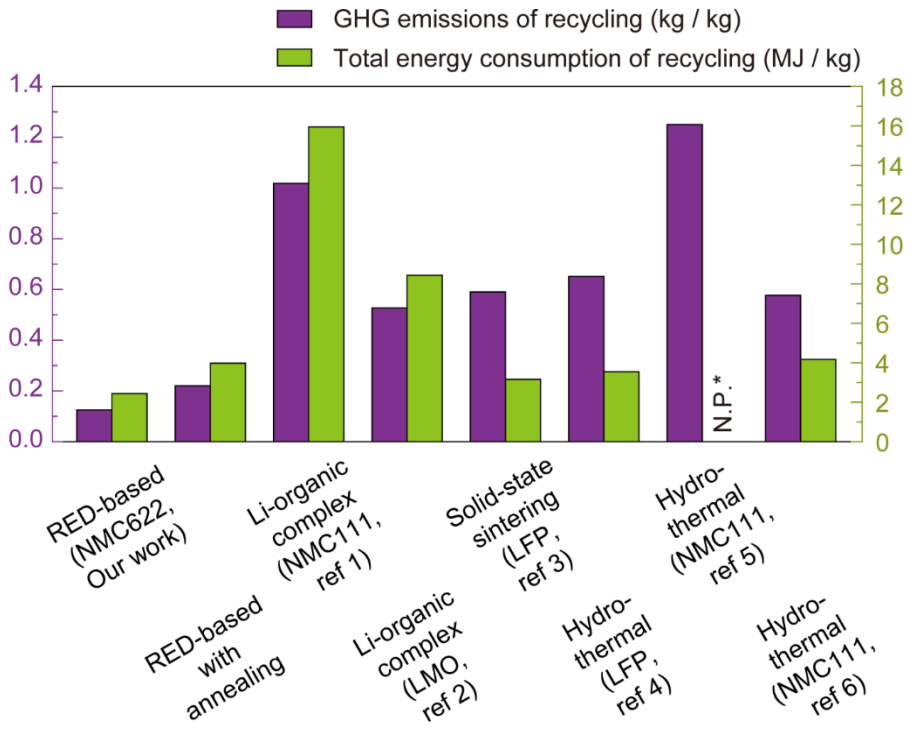

Fig. S49 Estimated GHG emissions and total energy consumption of our RED-based process for recycling 1 kg of spent battery cells. An additional calculation for the RED-based process with a post-annealing step (700°C, 2 hours, 5°C min^{-1}) is conducted to consider the potential for severe heterogeneity in microstructural degradation among cathode particles from practical spent batteries. The results are compared with those from other direct recycling methods in the literature as referenced below (N.P* indicates non-provided value from literature):

1. ACS Sustainable Chem. Eng. 2021, 9, 8214

2. Energy Stor. Mater. 2023, 55, 154

3. Nat. Commun. 2023, 14, 584

4. Joule 2020, 4, 2609

5. Adv. Energy Mater. 2023, 13, 2203093

6. Energy Stor. Mater. 2022, 51, 54

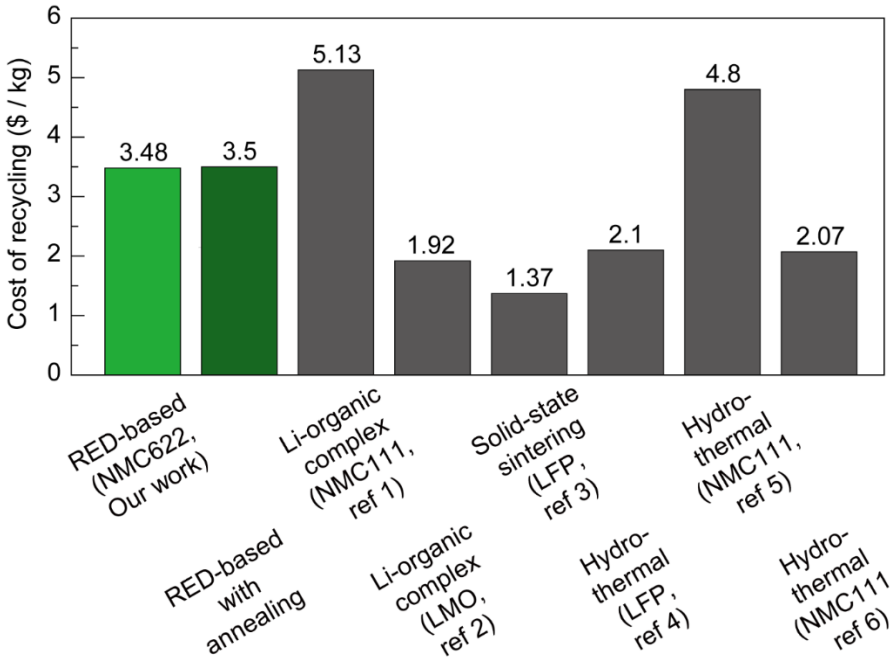

Fig. S50 Estimated costs of our RED-based processes including possible contribution from post-annealing step (700°C, 2 hours, 5°C min^{-1}) for recycling 1 kg of spent battery cells, compared with other direct recycling methods from literature referenced below:

1. ACS Sustainable Chem. Eng. 2021, 9, 8214

2. Energy Stor. Mater. 2023, 55, 154

3. Nat. Commun. 2023, 14, 584

4. Joule 2020, 4, 2609

5. Adv. Energy Mater. 2023, 13, 2203093

6. Energy Stor. Mater. 2022, 51, 54

Table S1-S16

Table S1. ICP-MS results for NMC622 cathodes at different electrochemical states. The 7.8% of Li content was irreversibly lost from "As-prepared" NMC622 during the first galvanostatic charge/discharge cycle. The Li-deficient NMC622 was prepared by galvanostatically charging "Fresh NMC" to 30% SOC. The chemical composition of "After regeneration" resembles that of "Fresh NMC", indicating the successful lithiation of Li-deficient NMC622 via a DMPZ-based thermodynamically driven lithiation reaction. The Li content of each electrode agrees well with the theoretical value calculated as below:

Sample	Li	Ni	Co	Mn
As-prepared	1.017	0.598	0.201	0.199
Fresh NMC	0.937	0.598	0.202	0.199
Li-deficient NMC (30% SOC)	0.722	0.595	0.203	0.201
Li-deficient NMC (100% SOC)	0.291	0.582	0.190	0.193
After regeneration	0.926	0.600	0.201	0.198

Theoretical capacity of NMC622: 276 mAh g^{-1} (1)

Irreversible capacity loss during 1st charge/discharge cycle: 20 mAh g^{-1} (2)

Reversible discharge capacity: 180 mAh g^{-1} (3)

Li contents of "As-prepared" = $\frac{(1)}{(1)}$ = 1, "Fresh NMC" = $\frac{(1)-(2)}{(1)}$ = 0.928, "Li-deficient NMC (30% SOC)" = $\frac{(1)-(2)-(3)*0.3}{(1)}$ = 0.732, "Li-deficient NMC (100% SOC)" = $\frac{(1)-(2)-(3)}{(1)}$ = 0.275, and "After regeneration" ≥ $\frac{(1)-(2)}{(1)}$ = 0.928

Table S2. Structural parameters obtained from the Rietveld refinement of XRD patterns of the fresh NMC622.

Element	x	y	z	Thermal factor (B)	Occupancy
O1	0.000	0.000	0.243 (0)	2.417 (172)	1
Co1	0.000	0.000	0.500	1.051 (105)	0.2
Mn1	0.000	0.000	0.500	1.051 (105)	0.2
Ni1	0.000	0.000	0.500	1.051 (105)	0.564
Ni2	0.000	0.000	0.000	2.000 (0)	0.036
Li2	0.000	0.000	0.500	1.051 (105)	0.036
Li1	0.000	0.000	0.000	2.000 (0)	0.964

Table S3. Structural parameters obtained from the Rietveld refinement of XRD patterns of the Li-deficient NMC622.

Element	x	y	z	Thermal factor (B)	Occupancy
O1	0.000	0.000	0.241 (33)	2.655 (210)	1
Co1	0.000	0.000	0.500	1.004 (125)	0.2
Mn1	0.000	0.000	0.500	1.004 (125)	0.2
Ni1	0.000	0.000	0.500	1.004 (125)	0.564
Ni2	0.000	0.000	0.000	2.000 (0)	0.036
Li2	0.000	0.000	0.500	1.004 (125)	0.036
Li1	0.000	0.000	0.000	2.000 (0)	0.769

Table S4. Structural parameters obtained from the Rietveld refinement of XRD patterns of the regenerated NMC622.

Element	x	y	z	Thermal factor (B)	Occupancy
O1	0.000	0.000	0.243 (0)	2.298 (173)	1
Co1	0.000	0.000	0.500	1.269 (111)	0.2
Mn1	0.000	0.000	0.500	1.269 (111)	0.2
Ni1	0.000	0.000	0.500	1.269 (111)	0.564
Ni2	0.000	0.000	0.000	2.000 (0)	0.036
Li2	0.000	0.000	0.500	1.269 (111)	0.036
Li1	0.000	0.000	0.000	2.000 (0)	0.964

Table S5. Atomic fraction of elements acquired from areal EDS analysis (area: 0.002 mm^2) of the regenerated NMC after rinsing process. The absence of nitrogen contents on the rinsed NMC indicates the complete removal of chemical residues that possibly originate from the regeneration solution containing RED (DMPZ) and Li salt (LiTFSI).

	Atomic %
C	62.57
O	17.07
F	13.28
Al	0.02
P	0.08
S	0.02
Mn	1.47
Co	1.40
Ni	4.09
Total	100.00

Table S6. The UV-vis absorbance intensities and calculated DMPZ concentrations of as-prepared and recycled DMPZ solutions. DMPZ concentrations were calculated using a standard calibration curve from **Supplementary Figure S20**.

Chemical state	Absorbance (a.u.)	DMPZ concentration (mmol L^{-1})
As-prepared (21 mmol L^{-1})	1.207	22.911
Recycled solution	1.250	23.730

Table S7. Peak assignments in FT-IR spectrum of DMPZ. The reversible changes of vibrational modes were related to the stretching of C=C and C–N–C bonds in the heterocyclic DMPZ molecules.

DMPZ

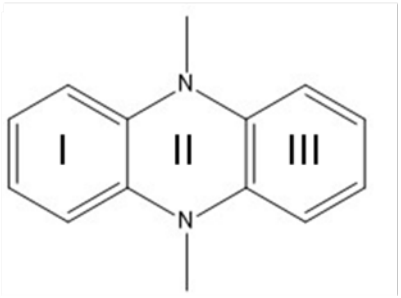

Wavenumber (cm^{-1})	Vibrational mode
1615	In-plane asymmetrical stretching of C=C bonds in ring I and III In-plane symmetrical stretching of C=C bonds in ring I and III
1476,1360	In-plane asymmetrical stretching of C-N-C bonds in ring II
1277	In-plane symmetrical stretching of C=C bonds in ring I and III In-plane symmetrical stretching of C-N-C bonds in ring II
1147	Rocking of methyl groups In-plane bending of H-C=C-H in ring I and III

Table S8. Comparison between conventional direct cathode regeneration methods and our RED-based strategy. [1, 9-21] Several existing approaches require harsh reaction conditions such as post-annealing over 800 °C for regeneration of NMC cathodes, or produce secondary chemical waste and pollution. In contrast, our RED-based strategy can regenerate various spent LIB cathode materials under ambient conditions (30 °C, 1 atm, and dry air) with minimal chemical waste. The pressure for hydrothermal methods was calculated as water saturation pressure at specific temperature. The non-available values are denoted as "-."

Method	***Cathode materials***	***V_{Li} quantification***	***Tempera-ture***	***Reaction time***	***Pressure***	***Inert atmosphere***	***Possible byproducts (or chemical waste)***	***Li demand***	***Post-annealing***	***Ref.***
Hydrotherm al	NMC111	X	220 °C	2 hours	23 bar	X	Strong alkaline solution (4 M metal hydroxide)	-	O	#6
	NMC532, NMC111		220 °C	4 hours	23 bar			-	O	#7
	NMC532, NMC111		220 °C	3 hours	23 bar			-	O	#8
	NMC622, NMC111		220 °C	4 hours	23 bar			-	O	#9
	NMC622, NMC111		100 °C	8 hours	1 bar			-	O	#10
	LMO		180 °C	6 hours	10 bar			570%	X	#11
	LFP		200 °C	3 hours	16 bar		Sulfuric acid or hydrazine	-	X	#12

	LFP, LMO		60–180 °C	3 hours	1–10 bar	O (annealing)	Alkaline solution, carbon dioxide (CO_2)	-	O	#13
Eutectic molten salt	LCO		500 °C	8 hours	Ambient pressure	X	Alkaline solution, CO_2	27200%	X	#14
	NMC532		>440 °C	5 hours				~105%	O	#15
	NMC532		400 °C	4 hours			Alkaline solution, nitrogen dioxide (NO_2), CO_2	~400%	O	#16
	NMC532		300 °C	>2 hours					X	#17
Li-arene complex	NMC622, LCO, LFP	O	30 °C	0.25 hour		O	Organic solvents with aromatic chemical reagents	100%	X	#18
	LMO		30 °C	0.5 hour		-		100%	X	#19
Our method	NMC622, NMC532 NMC811, LFP, LNMO, LCO	X	30 °C	0.25 hour		X	S, O_2	150%	X	This work

Table S9. Material requirements (kg) to recycle 1 kg of spent battery cells through pyrometallurgical (pyro), hydrometallurgical (hydro), and our RED-based process. During RED-based process, we assumed that all used reagents could be retrieved with a recovery rate of 90% through the solution recycling step. The non-available values are denoted as "-".

Material requirements (kg)	**Pyro**	**Hydro**	**RED-based**
Hydrochloric Acid	0.21	0.01	-
Hydrogen Peroxide	0.06	0.37	-
Limestone	0.3	-	-
Sand	0.15	-	-
Sulfuric Acid	-	1.08	-
Soda Ash	-	0.02	-
DME	-	-	18.74×10^{-3}
LiTFSI	-	-	0.46×10^{-3}
Ferrocene	-	-	0.28×10^{-3}
Lithium Sulfide	-	-	14.7×10^{-3}

Table S10. Energy requirements (MJ) to recycle 1 kg of spent battery cell through different process. Energy requirements for the pyrometallurgical (pyro) and hydrometallurgical (hydro) processes were obtained from default values established in the EverBatt 2020 for recycling NMC622 from spent LIBs. Energy requirements for the RED-based process are adopted from the previous paper, which demonstrated the direct regeneration under comparable condition (30 °C, 0.5 hour, and ambient pressure).[1] To include a post-annealing step in the RED-based process, we referred to the energy requirements from existing literature that demonstrated the direct regeneration under comparable conditions with some parameter adjustments to reflect the annealing time and temperature differences.[2]

Energy requirements (MJ)	**Pyro**	**Hydro**	**RED-based**	**RED-based (with 2-hour annealing at 700°C)**
Diesel	0.60	0.60	0.60	0.60
Natural gas	1.00	1.00	0.00	0.50
Electricity	1.18	0.13	0.13	0.62

Table S11. Value of recycled materials ($ kg^{-1}). All values are obtained from the EverBatt 2020. The non-available values are denoted as "-".

Recovered materials	**Pyro**	**Hydro**	**RED-based**
Aluminum	-	1.45	1.45
Copper	5.43	5.43	5.43
Graphite	-	0.2	0.2
Ni^{2+} in product	13.0	13.0	-
Mn^{2+} in product	-	3.0	-
Co^{2+} in product	52.0	52.0	-
Cathode product	-	-	20.6

Table S12. The life cycle inventory (LCI) obtained from the Ecoinvent V3 database for 1 kg of DME. The values of 'Global Warming Impact' and 'Cumulative Energy Demand' were used for calculating 'GHG emission' and 'Total energy consumption' of our RED-based strategy.

Impact Category	Unit	Values
Global Warming Impact	kg CO_2 eq.	2.44
Stratospheric ozone depletion	kg CFC11 eq.	7.03×10^{-7}
Ionizing radiation	kBq Co-60 eq.	0.137
Ozone formation, Human health	kg NO_x eq.	0.00509
Fine particulate matter formation	kg PM2.5 eq.	0.0029
Ozone formation, Terrestrial ecosystems	kg NO_x eq.	0.00539
Terrestrial acidification	kg SO_2 eq.	0.00634
Freshwater eutrophication	kg P eq.	0.00061
Marine eutrophication	kg N eq.	4.13×10^{-5}
Terrestrial ecotoxicity	kg 1,4-DCB	2.88
Freshwater ecotoxicity	kg 1,4-DCB	0.0998
Marine ecotoxicity	kg 1,4-DCB	0.129
Human carcinogenic toxicity	kg 1,4-DCB	0.151
Human non-carcinogenic toxicity	kg 1,4-DCB	1.79
Land use	m2a crop eq..	0.0315
Mineral resource scarcity	kg Cu eq.	0.00685
Fossil resource scarcity	kg oil eq.	1.48
Water consumption	m^3	0.0358
Cumulative Energy Demand	MJ	67.7

Table S13. The LCI for 1 kg of Li_2S obtained from the process data provided in Keshavarzmohammadian et al..[5] The values of 'Global Warming Impact' and 'Cumulative Energy Demand' were used for calculating 'GHG emissions' and 'Total energy consumption' of our RED-based strategy.

Impact Category	Unit	Values
Global Warming Impact	kg CO_2 eq.	4.13
Stratospheric ozone depletion	kg CFC11 eq.	1.51×10^{-6}
Ionizing radiation	kBq Co-60 eq.	0.202
Ozone formation, Human health	kg NO_x eq.	0.0147
Fine particulate matter formation	kg PM2.5 eq.	0.0107
Ozone formation, Terrestrial ecosystems	kg NO_x eq.	0.015
Terrestrial acidification	kg SO_2 eq.	0.0294
Freshwater eutrophication	kg P eq.	0.00337
Marine eutrophication	kg N eq.	0.00246
Terrestrial ecotoxicity	kg 1,4-DCB	13.6
Freshwater ecotoxicity	kg 1,4-DCB	0.314
Marine ecotoxicity	kg 1,4-DCB	0.409
Human carcinogenic toxicity	kg 1,4-DCB	0.779
Human non-carcinogenic toxicity	kg 1,4-DCB	9.09
Land use	m2a crop eq.	0.306
Mineral resource scarcity	kg Cu eq.	2.21
Fossil resource scarcity	kg oil eq.	1.42
Water consumption	m^3	0.0839
Cumulative Energy Demand	MJ	73.4

Table S14. The LCI for 1 kg of Fc obtained from the data provided in Griffiths et al..[4] The values of 'Global Warming Impact' and 'Cumulative Energy Demand' were used for calculating 'GHG emissions' and 'Total energy consumption' of our RED-based strategy.

Impact category	Unit	Values
Global Warming Impact	kg CO2 eq	10.9
Stratospheric ozone depletion	kg CFC11 eq	4.65×10^{-6}
Ionizing radiation	kBq Co-60 eq	0.654
Ozone formation, Human health	kg Nox eq	0.0224
Fine particulate matter formation	kg PM2.5 eq	0.055
Ozone formation, Terrestrial ecosystems	kg Nox eq	0.0232
Terrestrial acidification	kg SO2 eq	0.181
Freshwater eutrophication	kg P eq	0.00190
Marine eutrophication	kg N eq	3.57×10^{-4}
Terrestrial ecotoxicity	kg 1,4-DCB	12.8
Freshwater ecotoxicity	kg 1,4-DCB	0.534
Marine ecotoxicity	kg 1,4-DCB	0.683
Human carcinogenic toxicity	kg 1,4-DCB	0.643
Human non-carcinogenic toxicity	kg 1,4-DCB	8.18
Land use	m2a crop eq	0.122
Mineral resource scarcity	kg Cu eq	0.0373
Fossil resource scarcity	kg oil eq	6.48
Water consumption	m3	0.462
Cumulative Energy Demand	MJ	326

Table S15. The uncertainty analysis results for LCI of Fc.

Impact category	Unit	Mean	Median	SD	CV	2.50%	97.50%
Fine particulate matter formation	kg PM2.5 eq.	5.5E-02	5.5E-02	1.6E-03	2.87%	5.2E-02	5.8E-02
Fossil resource scarcity	kg oil eq.	6.49	6.5	0.113	1.74%	6.26	6.7
Freshwater ecotoxicity	kg 1,4-DCB	0.535	0.535	1.3E-02	2.50%	0.506	0.559
Freshwater eutrophication	kg P eq.	1.9E-03	1.9E-03	4.0E-05	2.11%	1.8E-03	2.0E-03
Global warming	kg CO_2 eq.	10.9	10.9	0.145	1.33%	10.6	11.2
Human carcinogenic toxicity	kg 1,4-DCB	0.644	0.644	1.4E-02	2.21%	0.613	0.67
Human non-carcinogenic toxicity	kg 1,4-DCB	8.19	8.19	0.194	2.37%	7.77	8.55
Ionizing radiation	kBq Co-60 eq.	0.655	0.654	1.3E-02	2.01%	0.631	0.68
Land use	m2a crop eq.	0.122	0.122	2.8E-03	2.26%	0.116	0.128
Marine ecotoxicity	kg 1,4-DCB	0.684	0.684	1.7E-02	2.49%	0.648	0.715
Marine eutrophication	kg N eq.	3.6E-04	3.6E-04	3.0E-06	0.83%	3.5E-04	3.6E-04
Mineral resource scarcity	kg Cu eq.	3.7E-02	3.7E-02	9.3E-04	2.49%	3.5E-02	3.9E-02
Ozone formation, Human health	kg NOx eq.	2.2E-02	2.2E-02	3.0E-04	1.33%	2.2E-02	2.3E-02
Ozone formation, Terrestrial ecosystems	kg NO_x eq.	2.3E-02	2.3E-02	3.1E-04	1.33%	2.3E-02	2.4E-02
Stratospheric ozone depletion	kg CFC11 eq.	4.7E-06	4.7E-06	6.3E-08	1.35%	4.5E-06	4.8E-06
Terrestrial acidification	kg SO_2 eq.	0.181	0.181	5.3E-03	2.95%	0.17	0.191

Terrestrial ecotoxicity	kg 1,4-DCB	12.8	12.8	0.273	2.14%	12.2	13.3
Water consumption	m^3	0.463	0.463	1.4E-02	2.98%	0.434	0.489

Table S16. The uncertainty analysis results for LCI of Li_2S.

Impact category	Unit	Mean	Median	SD	CV	2.50%	97.50%
Fine particulate matter formation	kg PM2.5 eq.	1.07E−02	1.08E−02	1.37E−03	12.7%	7.93E−02	1.34E−02
Fossil resource scarcity	kg oil eq.	1.43	1.43	0.171	12%	1.07	1.75
Freshwater ecotoxicity	kg 1,4-DCB	0.315	0.314	4.68E−02	14.8%	0.22	0.409
Freshwater eutrophication	kg P eq.	3.83E−03	3.36E−03	5.30E−04	15.7%	2.32E−03	4.41E−03
Global warming	kg CO_2 eq.	4.14	4.14	0.577	13.9%	2.97	5.28
Human carcinogenic toxicity	kg 1,4-DCB	0.78	0.777	1.21E−01	15.6%	0.536	1.02
Human non-carcinogenic toxicity	kg 1,4-DCB	9.1	9.07	1.4	15.4%	6.28	11.9
Ionizing radiation	kBq Co-60 eq.	0.202	0.202	2.94E−02	14.5%	0.142	0.261
Land use	m2a crop eq.	0.306	0.305	4.88E−02	15.9%	0.21	0.401
Marine ecotoxicity	kg 1,4-DCB	0.41	0.409	6.09E−02	14.9%	0.286	0.532
Marine eutrophication	kg N eq.	2.46E−03	2.45E−03	4.02E−04	16.4%	1.66E−03	3.24E−03
Mineral resource scarcity	kg Cu eq.	2.21	2.20	3.63E−01	16.40%	1.49	2.91
Ozone formation, Human health	kg NOx eq.	1.47 E−02	1.47E−02	2.22E−03	15.00%	1.02E−02	1.91E−02
Ozone formation, Terrestrial ecosystems	kg NO_x eq.	1.50E−02	1.49E−02	2.25E−03	15.00%	1.04E−02	1.95E−02

Stratospheric ozone depletion	kg CFC11 eq.	1.51E−06	1.51E−06	2.18E−07	14.40%	1.07E−06	1.95E−06
Terrestrial acidification	kg SO_2 eq.	0.0295	0.0295	3.67E−03	12.50%	0.0219	0.0364
Terrestrial ecotoxicity	kg 1,4-DCB	13.6	13.6	2.06	15.10%	9.47	17.7
Water consumption	m^3	0.0841	0.0842	1.16E−02	13.80%	0.0607	0.107

References

1. C. Wu, M. Xu, C. Zhang, L. Ye, K. Zhang, H. Cong, L. Zhuang, X. Ai, H. Yang and J. Qian, *Energy Storage Materials*, 2023, **55**, 154-165.
2. K. Park, J. Yu, J. Coyle, Q. Dai, S. Frisco, M. Zhou and A. Burrell, *ACS Sustainable Chemistry & Engineering*, 2021, **9**, 8214-8221.
3. G. Wernet, C. Bauer, B. Steubing, J. Reinhard, E. Moreno-Ruiz and B. Weidema, *The International Journal of Life Cycle Assessment*, 2016, **21**, 1218-1230.
4. O. G. Griffiths, J. P. O'Byrne, L. Torrente-Murciano, M. D. Jones, D. Mattia and M. C. McManus, *Journal of cleaner production*, 2013, **42**, 180-189.
5. A. Keshavarzmohammadian, S. M. Cook and J. B. Milford, *Journal of cleaner production*, 2018, **202**, 770-778.
6. R. Hischier, B. Weidema, H.-J. Althaus, C. Bauer, G. Doka, R. Dones, R. Frischknecht, S. Hellweg, S. Humbert and N. Jungbluth, *Final report ecoinvent v2*, 2010, **2**.
7. Y. Shi, G. Chen and Z. Chen, *Green Chemistry*, 2018, **20**, 851-862.
8. A. Manthiram, *Nature Communications*, 2020, **11**, 1550.
9. P. Xu, Z. Yang, X. Yu, J. Holoubek, H. Gao, M. Li, G. Cai, I. Bloom, H. Liu and Y. Chen, *ACS Sustainable Chemistry & Engineering*, 2021, **9**, 4543-4553.
10. Y. Shi, G. Chen, F. Liu, X. Yue and Z. Chen, *ACS Energy Letters*, 2018, **3**, 1683-1692.
11. Y. Guo, X. Liao, P. Huang, P. Lou, Y. Su, X. Hong, Q. Han, R. Yu, Y.-C. Cao and S. Chen, *Energy Storage Materials*, 2021, **43**, 348-357.
12. V. Gupta, X. Yu, H. Gao, C. Brooks, W. Li and Z. Chen, *Advanced Energy Materials*, 2023, **13**, 2203093.
13. X. Yu, S. Yu, Z. Yang, H. Gao, P. Xu, G. Cai, S. Rose, C. Brooks, P. Liu and Z. Chen, *Energy Storage Materials*, 2022, **51**, 54-62.
14. H. Gao, Q. Yan, P. Xu, H. Liu, M. Li, P. Liu, J. Luo and Z. Chen, *ACS applied materials & interfaces*, 2020, **12**, 51546-51554.
15. Q. Jing, J. Zhang, Y. Liu, W. Zhang, Y. Chen and C. Wang, *ACS Sustainable Chemistry & Engineering*, 2020, **8**, 17622-17628.
16. P. Xu, Q. Dai, H. Gao, H. Liu, M. Zhang, M. Li, Y. Chen, K. An, Y. S. Meng and P. Liu, *Joule*, 2020, **4**, 2609-2626.
17. J. Yang, W. Wang, H. Yang and D. Wang, *Green Chemistry*, 2020, **22**, 6489-6496.
18. G. Jiang, Y. Zhang, Q. Meng, Y. Zhang, P. Dong, M. Zhang and X. Yang, *Acs Sustainable Chemistry & Engineering*, 2020, **8**, 18138-18147.
19. Z. Qin, Z. Wen, Y. Xu, Z. Zheng, M. Bai, N. Zhang, C. Jia, H. B. Wu and G. Chen, *Small*, 2022, **18**, 2106719.
20. Y. Shi, M. Zhang, Y. S. Meng and Z. Chen, *Advanced Energy Materials*, 2019, **9**, 1900454.
21. C. Wu, J. Hu, L. Ye, Z. Su, X. Fang, X. Zhu, L. Zhuang, X. Ai, H. Yang and J. Qian, *ACS Sustainable Chemistry & Engineering*, 2021, **9**, 16384-16393.

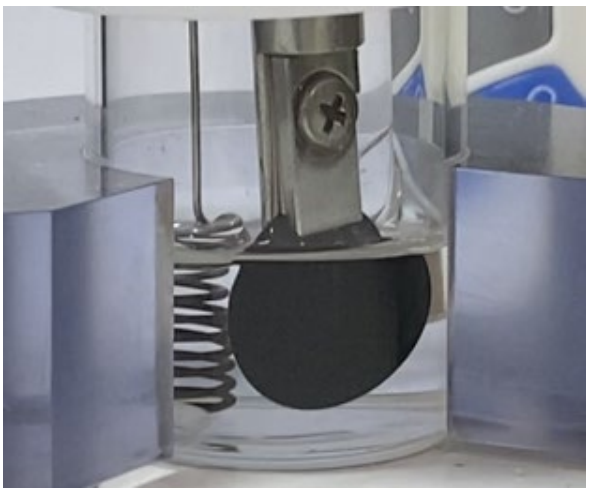

Video S1

: After injecting the DMPZ stock solution into the DME-based solution (containing only LiTFSI), DMPZ molecules are spontaneously oxidized to $DMPZ^{+}$, inducing the Li replenishment of a Li-deficient NMC622.